Applied Catalysis B: Environmental 327 (2023) 122434

Contents lists available at ScienceDirect

Applied Catalysis B: Environmental

journal homepage: www.elsevier.com/locate/apcatb

The effect of microscopic phenomena on the performance of iron-based oxygen carriers of chemical looping hydrogen production

Fabio Blaschke [a,*], Marjan Bele [b], Brigitte Bitschnau [c], Viktor Hacker [a]

[a] Institute of Chemical Engineering and Environmental Technology, Graz University of Technology, Inffeldgasse 25/C, 8010 Graz, Austria
[b] Department of Materials Chemistry, National Institute of Chemistry, Ljubljana 1000, Slovenia
[c] Institute of Physical and Theoretical Chemistry, Graz University of Technology, Stremayrgasse 9, 8010 Graz, Austria

ARTICLE INFO

Keywords:
Hydrogen production
Oxygen carrier
Chemical looping hydrogen
Steam-iron process
Microscopic phenomena

ABSTRACT

The scope of this work was to investigate and understand the microscopic effects on the performance of the active catalytic system in the chemical looping process. The inhibiting and accelerating effects of the different materials have been extensively studied. The ZrO_2 doped with MgO and Y_2O_3 showed a chemical inertness and the formation of a porous morphology for an enhanced cyclic stability. Testing in large-scale application indicates that supporting material with higher yttrium content in ZrO_2 has an excellent performance for 100 cycles. The HT-XRD and DSC analyzes clearly show microscopic phenomena play a fundamental role in the process and correspond to the phase transition. Stabilization of the cubic/tetragonal crystal structure leads to suppression of the phase transition and exhibits highest activity. The work reveals new fundamental principles for the design of OC in chemical looping hydrogen and understanding the influence of microscopic effects on the stability of oxygen carriers.

1. Introduction

The undeniable effects of climate change on the entire world is considered one of the greatest challenges facing humanity in the 21st century. New technologies in the field of energy production must therefore be developed or improved in order to combine competitiveness with the goals of reducing CO_2 emissions.

Against this background hydrogen is a promising alternative energy carrier due to its outstanding properties compared to other fuels [1,2]. It is a non-toxic gas with more than twice the energy density of gasoline. The combustion of hydrogen results in the formation of water vapor, which can be used in fuel cells [3,4]. This offers great potential for environmentally friendly clean energy production. In addition to its use as an energy carrier, hydrogen is needed primarily in the chemical industry. It is an essential base chemical for the production of ammonia and in refinery processes. Nevertheless, the footprint of hydrogen production must be considered. Unfortunately, over 99% of hydrogen is currently produced from fossil fuels (71% gas, 27% coal, 1% oil) [5]. The required high-purity hydrogen is mainly produced by methane reforming (C-SMR), which necessitates additional hydrogen purification steps [6]. This can be done primarily by pressure swing adsorption (PSA) or other techniques (absorption, cryogenic separation) that increase either the energy requirements or the capital costs of producing high-purity hydrogen. The production of hydrogen today consumes about 275 million tons (Mt) of oil equivalent energy, or 2.5% of the world's primary energy demand and results in a total CO_2 formation of about 830 Mt CO_2/year [7,8]. Due to gas shortages and supply chain problems caused by current international conflicts, the price of hydrogen is steadily increasing. The method by which hydrogen is produced is thus in need of an urgent change.

There are many ways to produce hydrogen from renewable resources. It can be produced by low or high temperature water electrolysis[9,10] or by gasification of biomass [11]. The basic prerequisite for the successful market establishment of regenerative processes is the cost per kg of hydrogen produced and the associated scalability for large-scale applications. The advantage of electrolysis is the high quality of the hydrogen with a purity of 99.999 vol% and its direct use for fuel cells [12]. However, water splitting requires a high-energy input. In addition, the environmental impact of hydrogen production by electrolysis is highly dependent on the available energy source. This increases the cost per kg of hydrogen and is not suitable for decentralized use.[13–15]. Above all, centralized hydrogen production has a significant impact on the environmental footprint of the fuel, in addition to the safety and economic aspects. Compared to natural gas, transporting

* Corresponding author.
E-mail address: blaschke@tugraz.at (F. Blaschke).

https://doi.org/10.1016/j.apcatb.2023.122434
Received 12 January 2023; Received in revised form 31 January 2023; Accepted 3 February 2023
Available online 4 February 2023

hydrogen through pipelines is not practical because it causes the type of mild steel used to become brittle and as a result can easily escape through the small holes in the material [16,17]. Therefore, centrally produced hydrogen must be transported long distances in tube tanks, which increases the carbon footprint and the final cost of hydrogen.

Compared to electrolysis, chemical looping technology (CL) is an elegant way to overcome the problem of long transport distances and high costs of hydrogen production. Other advantageous features include heat generation and carbon capture capability in one process [18,19]. A particular and innovative form of CL technologies for potential large scale decentralized green hydrogen production is the Reformer Steam Iron Cycle (RESC). Two reactor concepts for chemical looping hydrogen systems have been tested in the literature as potential operating systems: the fixed bed reactor and the fluidized bed or moving bed reactor [17,20,21]. The fixed-bed reactor has the advantage over the fluidized-bed reactor in that it is simple to operate and the system is compact and cost-effective for decentralized use. A brief explanation of the RESC process explains its advantages. In the first step, a hydrogen-rich syngas is produced by steam reforming from renewable hydrocarbons in the reformer, by steam-methane reforming (Eq. 1) and the parallel water-gas shift reaction (Eq. 2) leading to an equilibrium of CO, CO_2, H_2, and H_2O. The hydrogen-rich syngas is used for the stepwise reduction of an iron-based oxygen carrier (OC) in the second reactor part of the CL system (Eqs. 3, 4 and 5). The rich CO_2 stream can therefore be separated and stored with a carbon capture technology if needed. In the second step, steam is applied to the system to oxidize the iron while producing pure pressurized hydrogen (Eqs. 6 and 7). Thus, in this RESC process, green hydrogen can be stored and produced on demand through the cyclization of low-cost and environmentally friendly iron oxide.

Reforming step: $CH_4 + H_2O \rightarrow 3\ H_2 + CO$ (1)

$CO + H_2O \rightarrow H_2 + CO_2$ (2)

Reduction step: $3\ Fe_2O_3 + H_2/CO \rightarrow 2Fe_3O_4 + H_2O/CO_2$ (3)

$Fe_3O_4 + H_2/CO \rightarrow 3FeO + H_2O/CO_2$ (4)

$3\ FeO + 3\ H_2/CO \rightarrow 3Fe + 3\ H_2O/CO_2$ (5)

Oxidation step: $3\ Fe + 3\ H_2O \rightarrow 3FeO + 3\ H_2$ (6)

$3FeO + H_2O \rightarrow Fe_3O_4 + H_2$ (7)

Publications in the field of CLH provided a proof of concept for efficient large-scale production, purification and storage of hydrogen in a fixed-bed reactor by the use of synthetic biogas from production in a 10-kW fixed-bed chemical looping system with an Fe_2O_3/Al_2O_3 oxygen carrier pellet (80/20 wt%) [22]. The product gas quality had a purity of between 99.8% and 99.998%. A recent study with the same system showed the implementation under real conditions. A 10 kWth fixed-bed chemical looping system has been coupled directly to a 3 MWth biogas digester in the southern region of Austria. Green hydrogen with a gas quality of up to 99.998% was produced without using any additional downstream purification from agricultural residuals [23].

Despite the promising results, only the Fe_2O_3/Al_2O_3 80/20 wt% combination has proven to be a suitable oxygen carrier (OC) in large-scale applications for long-term operation. One of the key factors for the establishment of CL technology for hydrogen production in industry will mainly be the development of efficient new oxygen carriers with acceptable hydrogen production costs and high purity. Many advantages of different active materials have already been tested in the literature, but only iron-based oxygen carriers meet the criteria of high activity in the oxidation and reduction phases combined with low cost and environmental aspects [17,24,25]. However, pure iron-based oxygen carriers cannot meet the requirements without the addition of a support material. Due to the high degree of sintering of pure iron, the material is immediately deactivated in the reduction phase. This phenomenon reduces the oxygen exchange capacity and lowers the economy and usefulness for industrial applications. Therefore, different combinations of support materials were tested to keep the iron material active and ensure efficient hydrogen production over several cycle numbers. But also suppressing coke deposition for the production hydrogen with high purity [26]. During the oxidation and reduction phases at high temperatures, the OC is affected by many chemical and physical phenomena. By using the cheap support materials Al_2O_3, ZrO_2, and TiO_2, the stability and activity of iron in the process can be maintained over several cycles [17,27,28]. Nevertheless, material failure or other unexplained aspects occur in this material after a few cycles. For the Fe_2O_3/TiO_2 combination, a higher content of support material in the range of 30–40% was required to ensure stable operation in the reactor for more than 10 cycles [29,30]. It should be noted that adding higher proportion of support material, decreases the specific hydrogen production (SHP) of the process. This reduces the economic balance of OC, which is associated with a higher hydrogen production price per cycle. If an Al_2O_3 is used instead of TiO_2, the cycling stability of iron-based oxygen carriers can be stabilized with a lower amount. Recent work has shown that Fe_2O_3/Al_2O_3 in a mixture of 80/20 wt% can be used over 100 redox cycles with good mechanical stability [27]. However, characterization of OC has shown that the Al_2O_3 interacts with the iron oxygen carrier during cycling. The support material leads to the unreactive formation of hercynite ($FeAl_2O_4$), which negatively affects the utilization of the high hydrogen production rate [31]. An alternative idea to improve the capacity of the reduction, was doping the OC. Especially doping of hexaaluminates with Fe-substituted lanthanum-hexaaluminates show a significant increase of the reactivity of 50 redox cycles in a fixed-bed reactor with 0.2 g OC amount [32]. In addition hexaaluminates has the benefit of a targeted A-site doping of the perovskite structure with e.g. Sr, which led to better oxygen donating ability. This results in faster kinetics by suppress the carbon deposition at the same time [33]. Another approach is the doping of iron OC with Ni in order to form a $NiFe_2O_4$ via a sol-gel method. The H_2 production capacity of the mixed OC ($NiFe_2O_4 + Al_2O_3$) was stable in 1 g scale within the 20 cycles, because of avoiding particle sintering and deactivation. [34] Nevertheless, large quantities of Al_2O_3 in a content of 40 wt.-% were needed, to keep the spinel structure active. A further problem is that nickel-polluted environments can cause a variety of side effects on human health, such as allergy, kidney diseases, lung fibrosis, lung and nasal cancer [35]. Apart from the higher cost of using nickel to improve the process, the impact on human health and the environment makes this approach unattractive for green hydrogen production. An alternative could be ZrO_2 as support material. A mixture of 30 mol% ZrO_2 and 70 mol% Fe_2O_3 prepared by the co-precipitation method leads to stable operation of 20 cycles at 850 °C. An indication therefore is the observation that no chemical interaction was detected [36]. This indicates that no side phase or uncreative compound of Fe_2O_3 forms with the support material during the process [37]. Good results were also achieved with iron oxide stabilized with yttrium-stabilized zirconia, which was prepared using the sol-gel method. An OC composition of Fe_2O_3/YSZ-20 70/30 wt.-% in 0.5 g scale yield in hydrogen production of ~10.30 mmolH_2/gOC for 20 cycles [38]. However, we see no future for this OC manufactured method in-scale large applications. Sol-gel synthesized oxygen carriers prepared with nitrate salts are toxic and expensive methods. For CL, the many precipitation and purification steps of the synthesis method present a major challenge in producing larger quantities and are unattractive for production at OC. In addition, it is important to emphasize that the authors have not presented a study in which this material was used in a larger sample size. With the exception of Al_2O_3 as support material, all other materials were tested only in mg or in up to 1 g scale in form of powder as reactor batch. Additionally, a high number of total cycles over 20–30 was not shown. This is important, because Zacharis et. al have shown in their work that the results of the TGA investigations in particular in the form of powder, deviate greatly from large-scale applications [27]. In their TGA experiments on an iron-based powder sample containing only 5 wt.-% Al_2O_3 a

high oxygen exchange capacity due to the small content of an inert support material was shown in up to 100 cycles. However, to operate the RESC system in large-scale application, the material must be brought into a textured shape such as pellets, to prevent a pressure drop inside the system. Testing of this material in a 250-g fixed-bed reactor resulted in disintegration of the pellets and clogging of the reactor after 30 cycles. An explanation of what is happening here at the microscopic level has not been shown. To the best of the author's knowledge, this is the reason why until now only an OC with the composition Fe_2O_3/Al_2O_3 80/20 wt % in pellet form via dry mixing, was able to reach pellet lifetimes of over 100 cycles in large scale of 250 g in fixed-bed systems or larger.

Considering the results of the above studies, it became clear that new material compositions for large-scale application of fixed-bed reactors are urgently needed to advance the technology. This is important for the possible upcoming industrial implementation of such chemical looping systems with sufficiently high hydrogen production over a large number of cycles for low-cost green hydrogen production. In addition, detailed characterization and fundamental understanding of the microscopic-level effects that influence the process for efficient mg-scale material screening and subsequent upscaling to pellet form for large-scale fixed-bed reactor systems are of great importance. The carbon deposition affects the process and could cover up a distinction from other microscopic phenomena. Therefore, pure hydrogen is used as the reducing agent in order to be able to characterize additional microscopic phenomena between the iron and the support material. This enables the precise determination between the SHP and microscopic phenomena. Therefore, the study focuses on iron oxide-based OC in the form of Fe_2O_3 as the starting material mixed with 20 wt.-% support material to achieve a good combination of stability and high specific hydrogen production. All materials are produced by the dry mixing method to provide a fast, simple, and low-cost fabrication method that can be easily scaled up. TiO_2, Al_2O_3 and ZrO_2 are used as support materials because they are environmentally friendly, inexpensive and available in larger quantities. Alumina with two different particle sizes is used to show that particle size does not affect the process. The focus is on ZrO_2-based support materials to prevent the formation of an unreactive side phase. Other doped ZrO_2 materials are being investigated to take advantage of the doping material properties such as structural stability. It is known from other research areas, such as ceramic engineering, that pure ZrO_2 leads to catastrophic fractures at elevated temperatures in ceramic devices, resulting in structural unreliability [39]. Therefore, commercially available ZrO_2 stabilized with CaO, MgO and Y_2O_3 in different concentrations is used. The idea is that the so-called mixed ionic electronic conductors (MIECS) stabilize the ZrO_2 phase and lead to advantageous properties. To compare the differences between the material classes, a detailed material screening is first performed by Thermogravimetric analysis of the sample structure. The materials will be compared in terms of their oxidation, reduction and hydrogen production performance on a small scale. The goal is to understand the differences of the base material and the influences of the doping material on the process, such as the formation of unreactive side phases, particle size and shape, and sintering phenomena. Second, the most promising candidates will be tested in a fixed-bed reactor with a 250 g quantity of OC. The cycle experiments are carried out in long-term operation with up to 100 redox cycles each. In particular, Fe_2O_3/Al_2O_3 80/20 wt% serves as a benchmark, since it is the only material composition known in the literature for a large-scale application. The aim is to find a new OC composition that outperforms the benchmark Fe_2O_3/Al_2O_3 80/20 wt% for 100 cycles. In addition, conclusions will be drawn on the influence of various phenomena such as the formation of secondary phases, changes in crystal structure and surface morphology, and particle size and shape on the influence of hydrogen generation in the chemical looping process to determine the properties for a successful support material in CL.

This work demonstrates the importance of microscopic phenomena on the performance of the active catalytic iron system of the process and provides a new approach to the design of the oxygen carrier for large-scale systems. Especially the lattice match of Fe_3O_4/Fe and the crystal structure change of the support material were characterized as important phenomena for efficient H_2 production in CL large-scale applications. The use of yttrium doped ZrO_2 in higher concentration avoid the pulverization of the oxygen carrier in the fixed bed chemical looping hydrogen system by developing and optimizing the support material. The material combination of Fe_2O_3 stabilized with YSZ show excellent SHP of 10 molH_2/kgOC for 100 cycles. In particular, both microscopic and macroscopic phenomena affecting the entire process were found and explained.

2. Experimental

2.1. Synthesis of the oxygen carrier samples

In the present work a reaction set-up of oxygen carriers were prepared in a fixed weight ratio of Fe_2O_3 powder (Thermo scientific) stabilized with support material in the weight ratio of 80:20 wt.-%. The method of mechanical mixing was used to synthesize the oxygen carrier. The OC was temperature treated in air for 6 h at 900 °C. The following support material was used: 1 μm Al_2O_3 (α -phase, Alfa Aesar), 50 μm Al_2O_3 (α -phase, Alfa Aesar), TiO_2 (anatase Alfa Aesar), ZrO_2 (Alfa Aesar), calcium stabilized zirconium oxide with 4% CaO (Alfa Aesar), yttria stabilized zirconium oxide with 3 mol% Y_2O_3 (Treibacher Industrie AG), yttria stabilized zirconium oxide with 8 mol% Y_2O_3 (IK-Hochrhein) and yttria stabilized zirconium oxide with 10–15 mol% Y_2O_3 (Alfa Aesar) and magnesia stabilized zirconium oxide with 10 mol% MgO. The magnesia stabilized zirconium oxide is prepared with a solid solution method, preparation procedures were reported in previous work [40]. The following abbreviation was used as an abbreviation for the OC mixture, Fe_2O_3 with the respect support material in the weight ratio of 80:20 wt.-%: 1 μm Al_2O_3, 50 μm Al_2O_3, TiO_2, ZrO_2, ZrO_2 +CaO, YSZ3, YSZ8, YSZ10 and ZrO_2 +MgO. The pelletized oxygen carrier samples with a diameter of 2–4 mm were formed in a high-performance mixing system (Eirich EL1) with distilled water. After granulation, the OC was temperature treated in air for 6 h at 900 °C.

2.2. Thermogravimetric analysis

Thermogravimetric analysis was performed with a Netzsch STA 449 C Jupiter, equipped with a water vapor furnace and a steam generator (aDROP). Measurements were performed in a corundum plate sample carrier using 40 mg oxygen carrier powder. The experimental cycle consists of reduction, purge and oxidation phase. A TPR analysis was carried out at the beginning and end of each of the 10 cycles with heating rate of 10 K/min, the total gas flow of 50 mL min^{-1} H_2 and 100 mL min^{-1} N_2. The reduction set time was 30 min with a total gas flow of 50 mL min^{-1} H_2 and 100 mL min^{-1} N_2 at 800 °C. The purge phase has a duration of 5 min with 100 mL min^{-1} N_2. The oxidation set time was 30 min with 2.44 g min^{-1} steam supply and carrier gas flow of 100 mL min^{-1} N_2 at 800 °C. Oxygen exchange capacities were calculated from the difference of the median from the purge phases after oxidation and reduction in order to create the same gas atmospheric conditions in both the reduced and oxidized state.

2.3. Characterization

X-ray diffraction (XRD) powder diffraction was carried out with an XRDynamik (Anton Paar) with Bragg-Brentanogeometry and Cu-Kα radiation source. The sample was scanned at a scanning rate of 400 s/step in dynamic range from $2\theta = 8–100°$. The XRD peaks were assigned using the inorganic crystal structure database (ICSD). Scanning electron microscopy (SEM) analysis was performed with a Philips XL20 device. Differential scanning calorimetry (DSC) analysis was performed with a Netzsch STA 449 C Jupiter with a heating and cooling rate of 15 K/min with a sample holder type S and in corundum crucible. The sample

amount was 12 mg support material powder. The measurement was performed under nitrogen atmosphere with a gas flow of 100 mL min^{-1} N_2.

Scanning electron microscopy (SEM) and SEM with energy dispersive X-ray analysis (SEM/EDX) were carried out using a field emission SEM Zeiss Supra TM35 VP (Carl Zeiss AG, Oberkochen, Germany), equipped with an EDX spectrometer - silicon drift detector EDX UltimMax 100 (Oxford Instruments, Oxford, UK).

Structural changes during reduction at high temperature were monitored by temperature-programmed powder high-temperature X-ray diffraction measurements on a PANalytical X'Pert PRO high-resolution diffractometer (PANalytical B.V., Almelo, Netherlands) with alpha1 configuration (CuKα1 λ = 1.5406 Å radiation). Diffractograms were recorded with a step size of 0.039° and an integration time of 100 s in the 2θ range from 15° to 75° using a fully open scanning X'Celerator detector. Measurements were performed at 800 °C, first in Ar atmosphere and then in Ar/H_2(5%) atmosphere after the first measurement (11 min). The gas flow was kept constant at 150 cm^3 min^{-1}. Phases were identified using the X'Pert HighScore Plus programme and the International Centre for Diffraction Data (ICDD) PDF-4 + 2021 database.(a) a) Gates-Rector, S.; Blanton, T. The Powder Diffraction File: A Quality Materials Characterization Database. Powder Diffr. 2019, 34 (4), 352–360. https://doi.org/10.1017/S0885715619000812.

2.4. Fixed bed reactor experiments

A tubular fixed bed reactor setup was employed for the oxygen carrier characterization via cyclic reduction and oxidation of oxygen carrier pellets. The reactor pipe with an inner diameter of 44 mm and a length of 70 cm was heated externally via an electric furnace (Carbolite Gero) at 800 °C. The determination of the SHP was realized gravimetrically via positioning the fixed bed reactor vertically on a precision scale (Kern ILS 30 K/4 C). The temperature development over the consecutive redox cycles was logged with a thermocouple (Type K), which was positioned in the center of the oxygen carrier bed. For the test series 250 g of pelletized oxygen carrier was placed in between inert alumina pellets (Alfa Aesar), which were used for gas preheating and vertical stabilization of the oxygen carrier bed (Fig. 8). Gases and liquids were added in using mass flow controller from Bronkhorst. The reduction was carried out with 15 NL min^{-1} pure hydrogen for 36 min and the oxidation with 8 g min^{-1} steam for 20 min. After each redox cycles the reactor was purged with 5 NL min^{-1} nitrogen for 3 min Between the cycle tests in the fixed-bed reactor on the measurement days, the OC was stored in the reduced state in the reactor under an inert nitrogen atmosphere.

3. Results and discussion

3.1. Thermogravimetric analysis

The hydrogen production and storage performance of the different materials were investigated using TGA. Detailed screening of the materials over 10 cycles at 800 °C was done (see Fig. S1). The powder screening provides detailed information on reduction, oxidation and hydrogen production. First, the experimental data were used to determine SHP, which indicates the number of moles of hydrogen produced per total OC quantity (see S1 for the calculation). This is a specific value to represent hydrogen production and is important for comparing different OCs with respect to large-scale applications. The higher the value SHP, the more hydrogen that can be produced or stored with the same quantity of material. This screening method can give a good overview of the cyclic performance of the different support materials over the cycle time. The SHP value of each cycle was calculated from the mass exchanged during the reduction and oxidation cycles. The results of the SHP values are shown in Fig. 1. Note that a TPR analysis was performed in the first step. The samples were first completely reduced from Fe_2O_3 to Fe using hydrogen. The initial determination of SHP begins with the oxidation. Due to thermodynamic properties, Fe can only be oxidized back to Fe_3O_4 and not completely to Fe_2O_3. The screening experiments show a significantly different behaviour of the material over 10 cycles. The group consisting of the materials TiO_2, Al_2O_3 with different particle size and ZrO_2 doped with CaO shows a decrease in SHP performance with increasing number of cycles (group 1). Compared to group 2, the material with pure ZrO_2 doped with Y_2O_3 and MgO shows good SHP stability over 10 cycles in the range of ~12.7 mmol H_2/ gOC, which is 16% higher SHP than the values known from literature, which can be attributed to a lower mass ratio of the support material [38]. No obvious decrease in H_2 production with increasing cycle number was observed. In comparison, the group 1 materials have a significantly lower overall value of SHP compared to group 2 of about 5% after 10 cycles. Due to the addition of dopants, the MIECs exhibit no higher hydrogen production than pure ZrO_2. The values are between the standard deviation of the TGA system. Thus, no significant differences are observed within the ZrO_2 support material (the exception is the sample doped with CaO). A different effect of doping with alkaline earths was observed. CaO doping has a negative effect on the ZrO_2 support structure, while MgO in combination with ZrO_2 support material has a positive effect on the SHP value. The ZrO_2 +CaO exhibits the

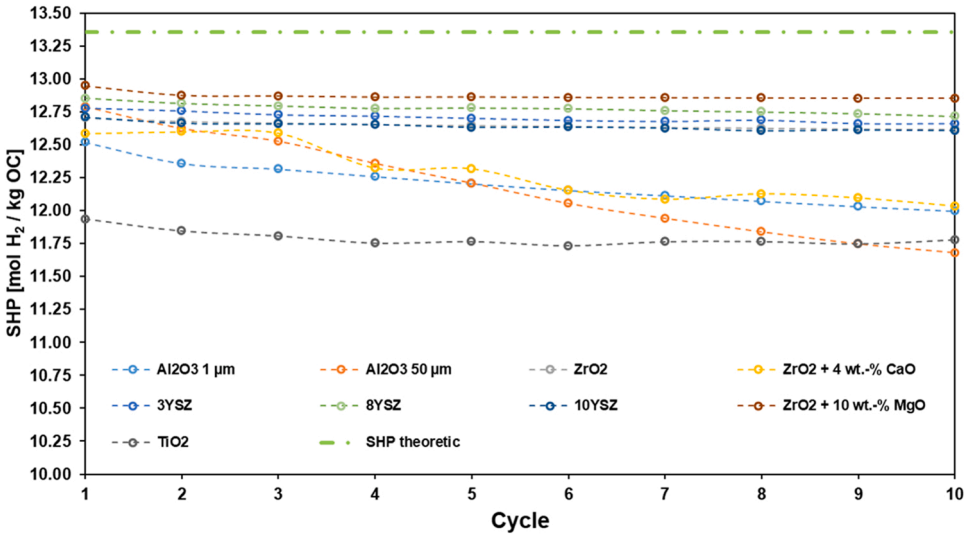

Fig. 1. Comparison of the specific hydrogen production values of Fe_2O_3 with different support material in ratio the 80/20 wt.-% at 800 °C for 10 cycles.

lowest value in the series of ZrO_2-doped support materials. The values of the Al_2O_3 support additive show that varying the particle size does not lead to any advantage. Both particle sizes show reduced cycle performance. As the third base material, the TiO_2 shows a stable SHP over 10 cycles. Nevertheless, the material has the lowest overall SHP values below 12 molH_2/kgOC. The initial values are lower compared to all other base materials. The results indicate that ZrO_2 materials, especially the MIECs (except CaO), have some positive properties on H_2 production and storage performance, and exhibit stable oxidation and reduction behaviour of the iron oxygen carrier.

3.2. *Effects of the support material on the reduction and oxidation performance*

Based on the different behaviours of the materials during H_2 production, the influence of the support material on the reduction and oxidation performance at 800 °C was also studied in detail. These data provide results to determine whether reduction or oxidation leads to degradation of SHP. The material was reduced and oxidized 10 times at 800 °C. The 1st and 10th cycles were taken as examples for each material to determine the change in reaction behaviour over the number of cycles. The degrees of oxidation and reduction were calculated using the theoretical values for each OC. A degree of oxidation of 0 means that the sample is completely reduced to Fe, and 1 means that all the iron is oxidized to Fe_3O_4. The reverse is true for the reduction degree values. Fig. 2 shows the oxidation rate and Fig. 3 the reduction rate of all materials (a) in the first cycle and (b) in the tenth cycle, over the entire reaction time and for zoom spectra of the first 350 s see (c) for the 1st and in (d) for the 10th cycle. The characteristic changes are graphically highlighted by the orange boxes with numbers in combination with dashed blue arrows. In the 1st cycle of oxidation, it can be seen that all materials based on Al_2O_3 and ZrO_2 exhibit a fast oxidation rate. In about 180 s, more than 90% of the OCs are completely oxidized, only the CaO doped ZrO_2 slows down for 20 s, but it is still fast. Fe- OC stabilized with TiO_2 leads to a slow release of hydrogen. In point 3 Fig. 2(a) it is shown that 90% of OC is oxidized only in 1220 s, which is 6 times slower

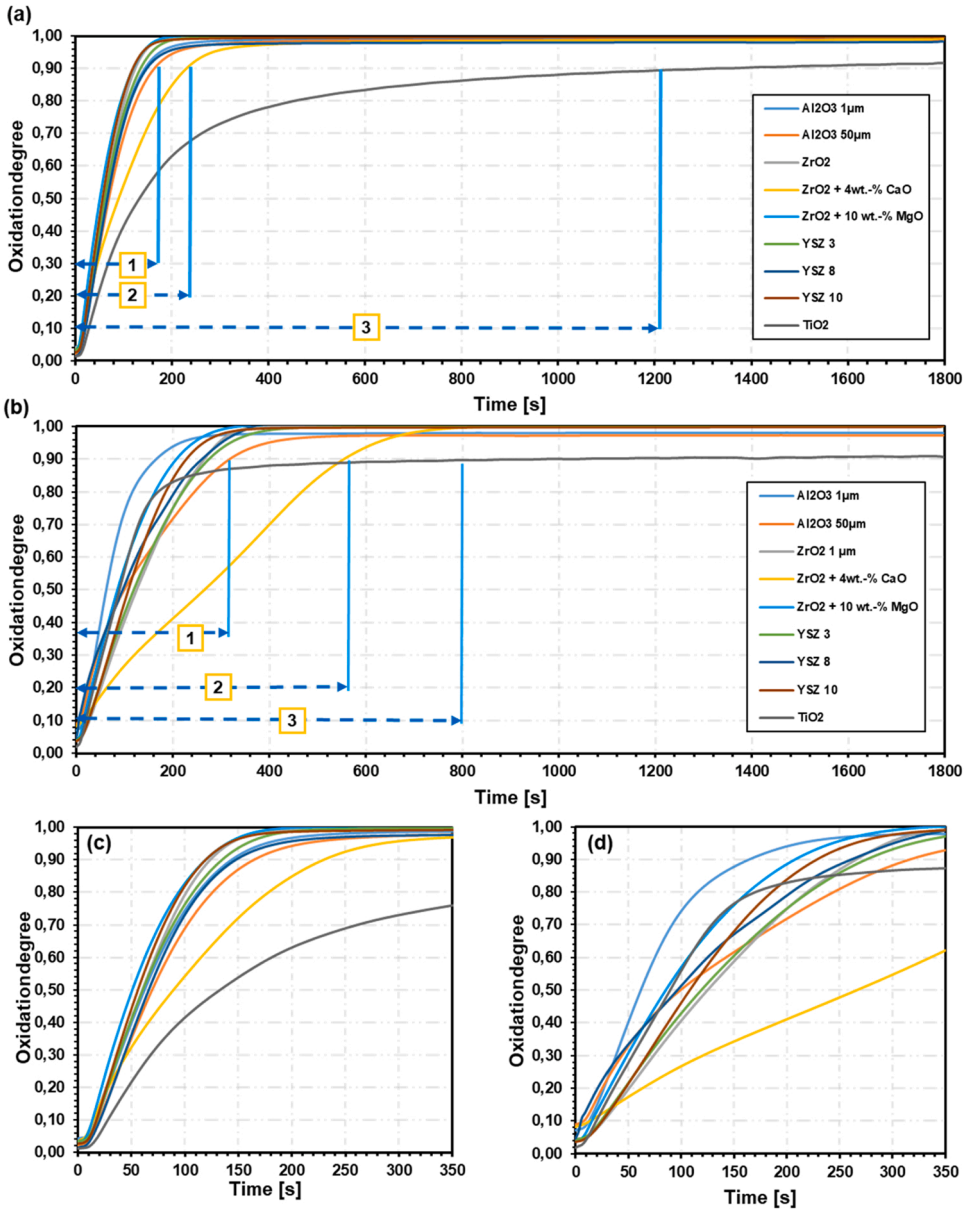

Fig. 2. Comparison of the oxidation rate of the different OCs - Fe_2O_3 with support material in the weight ratio 80/20 wt.-% at 800 °C in a.) the 1st and in b.) the 10th cycle of oxidation. In c.) zoom spectra of the 1st and in d.) zoom spectra of the 10th cycle of oxidation.

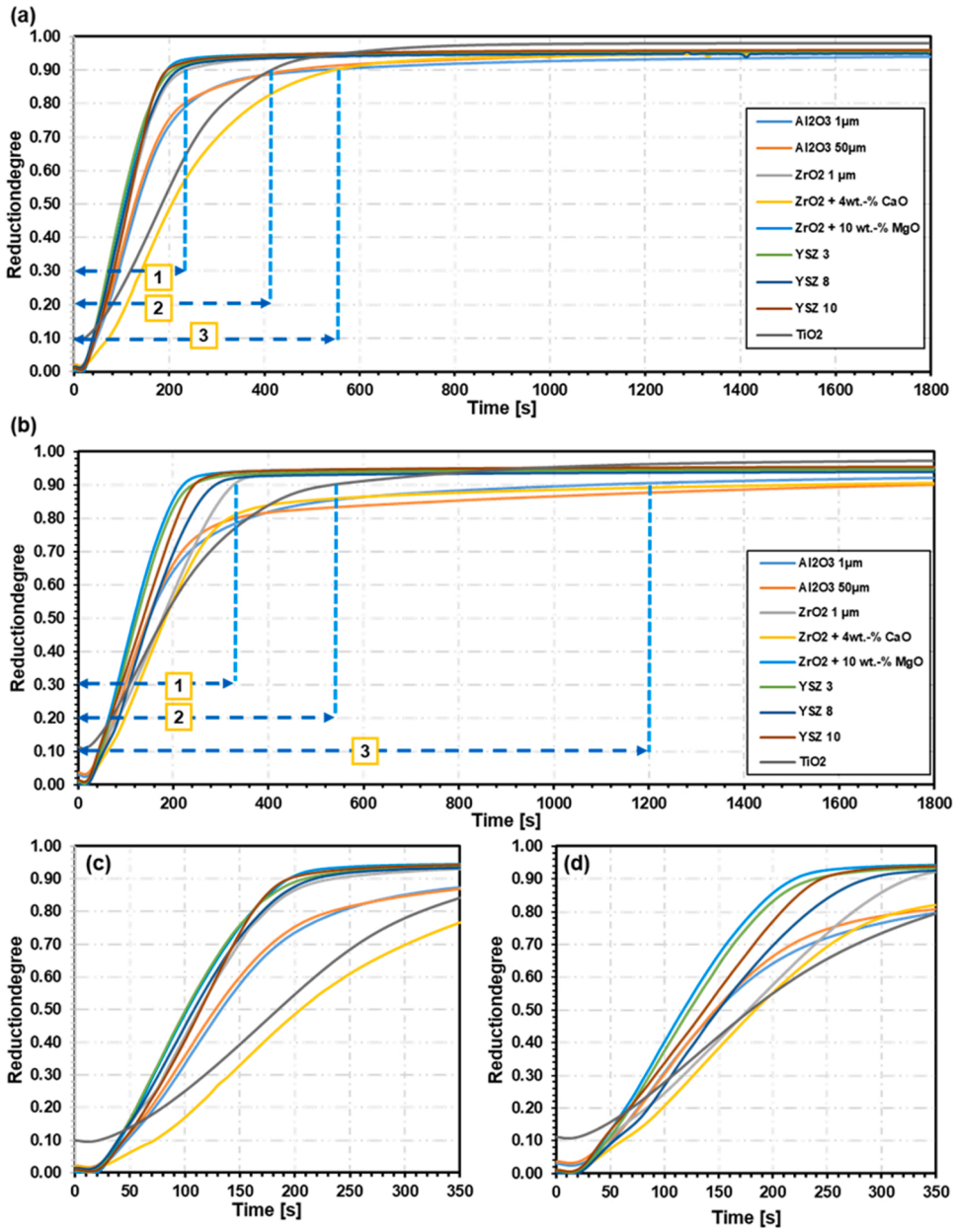

Fig. 3. Comparison of the reduction rate of the different OCs - Fe_2O_3 with support material in the weight ratio 80/20 wt.-% at 800 °C in a.) the 1st and in b.) the 10th cycle of oxidation. In c.) zoom spectra of the 1st and in d.) zoom spectra of the 10th cycle of reduction.

oxidation rate per second than ZrO_2 and Al_2O_3 OC. It was also observed that the sample stabilized with TiO_2 was not able to oxidize completely within 30 min. Thus, an oxidation rate of 90% was achieved. This is the first indication for the lower SHP value of the TiO_2 support material. Fig. 2(b) and (d) shows the oxidation behaviour in the 10th cycle. A closer look at the starting point of the Al_2O_3 material with a particle size of 1 µm and 50 µm and the ZrO_2-CaO support material shows that the oxidation rate starts at 0 s for an oxidation value of 0.06–0.09 in cycle 10. This means that 6–9% of the material could not be fully recovered during the reduction cycle. A comparison of the orange boxes numbered 3 in Fig. 2(a) and (b) also shows that the oxidation performance of some support materials changes dramatically over the number of cycles. The point 1 (b) shows the pure ZrO_2 and materials doped with MgO, YSZ3, YSZ8, YSZ10, Al2O3 1 µm & 50 µm maintain their fast oxidation behaviour. The results also show using Al_2O_3 with a different particle size does not result in a faster reaction tendency with water over the number of cycles. Again, a different behaviour is seen for ZrO_2 doped with CaO in the 10th cycle, where the oxidation rate for the value of 90% changes from 220 s to 560 s from cycle 1 to cycle 10. This also shows that some changes have occurred in the morphology of the material. However, ZrO_2 can be completely oxidized with CaO even in 680 s. This indicates that the deteriorations at SHP probably occur in the reduction phase compared to the other ZrO_2 materials. TiO_2 shows an opposite behaviour compared to the other materials. In cycle 10, the oxidation rate is accelerated compared to cycle 1. The value of 90% is reached in about 800 s. Compared to cycle 1, this is an improvement of 400 s. Nevertheless, it has the slowest oxidation rate. The results show, TiO_2 has the worst oxidation performance, while ZrO_2 (exception: doped with CaO) and Al_2O_3 are excellent support materials for the rapid release of hydrogen with water vapour.

In addition, a high and fast reduction rate is an important factor for efficient hydrogen storing value in the form of pure iron, which can then theoretically be completely released subsequently in the oxidation cycle. Fig. 3 shows the reduction rate of all materials for (a) + (c) 1st cycle and

in the (b) + (d) 10th cycle. The characteristic changes of the OCs due to the influence of the different support materials are again represented by the marked dots in the orange boxes. However, obvious differences can be seen between the progressive cycle numbers of the OC samples. It should be noted that the TiO_2 sample starts at a reduction ratio of 0.11 (see Fig. 3d). From the results obtained from Fig. 2, it can be seen that the titanium-based iron substrate OC only reaches a value of about 90% in the oxidation phase. All other samples start at a reaction degree of ~ 0.00. For the first cycle, the ZrO_2-based materials have the fastest reduction performance, except for CaO-doped ZrO_2, compared to all other support materials. The stabilization of the iron-oxygen support allows to reach the 90% reduction mark under 240 s (see Box 1 in Fig. 3 (a) and (c). The Al_2O_3 samples show a fast reaction rate with the hydrogen gas in the first stage up to the 70% reduction level. After that, the reactivity decreases and the reduction flattens out, resulting in 90% of the iron oxide being reduced in 560 s. No difference was observed between the particle sizes of Al_2O_3 in the first cycle. The TiO_2 and ZrO_2-CaO samples also show slow reactivity. Although Al_2O_3 shows a higher reaction rate at the start, the TiO_2 sample reaches the 90% value in 410 s like the aluminium samples (Fig. 3(a) point 2).

In Fig. 3(b) the reaction behavior in the 10th cycle of reduction is displayed. Based on the results, the samples consisting of ZrO_2 demonstrate again a perfect reduction performance with the exception of CaO. No loss of the SHP due an insufficient reduction in 30 min is detected. In Fig. 3. (b) point 1 and (d), a reduction degree of 90% is reached in under 320 s. Small difference can be detected for ZrO_2 without any dopant the reduction rate is slightly decreased. In Fig. 3 point 2 (b) the TiO_2 reaches the value of 0.9 reduction degree in 520 s and can achieve a high reduction rate within 30 min compared to Al_2O_3. Nevertheless, it should be noted again by comparing the results, that the OC with titanium, starts at reduction degree around 11%, which explain the faster reduction to Al_2O_3. In point 3 (b) show Al_2O_3 and ZrO_2-CaO have a lack of performance in the reduction phase and TiO_2 in the oxidation phase. The reduction performance crashed dramatically down after 10 cycles. The reaction degree of ~0.90 can be reached in 1200 s. In addition, the reaction time of 30 min with hydrogen is not sufficient to fully reduce the Al_2O_3 and CaO doped sample and therefore start at a higher value rate of oxidation, which was discussed in Fig. 2(b). The results in differences of the earth alkali dopant show for the reduction data the same phenomena like in the oxidation. The MgO leads to a fast oxidation and a fast reduction behavior, the CaO dopant impair the properties of ZrO_2 support material. In summary the results preliminarily indicate that high values of SHP for pure ZrO_2 and doped with YSZ and MgO are attributed to the excellent behavior in oxidation and reduction stability over the number of cycles.

3.3. Comparison of TPR data with the reduction, oxidation and SHP performance

The influence of the reactivity of different support material on the iron based oxygen carrier was investigated by TPR (temperature-programmed reduction) analysis to obtain a deeper understanding of what happens during the reduction phase. The DTG curve was obtained from the TGA data set by the first deviation. Therefore, different side compounds and also possible reaction mechanisms, which are formed due the cycle number, can be made visible. The TPR was performed before and after the cyclisation of each material. These experimental results are shown in Fig. 4 for the uncycled sample and in Fig. 5 for the cycled sample after 10 cycles. For a better overview, the support materials have been divided into two charts. The good performing OCs are displayed in Figs. 4 and 5 respectively in (a) and (b). The OCs with a decreased reduction, oxidation or hydrogen production performance are for Figs. 4 and 5 in (c) and (d); as a comparison between the material classes, the MgO sample is additionally plotted again in (c) and (d). In Fig. 4 the TPR results show two peaks for all sample were detected, with the exception of TiO_2. The smaller peak at 380 °C belongs to the Fe_2O_3, which reacts with the hydrogen at lower temperature to Fe_3O_4. The followed reaction are shifted to higher temperature since a lower oxidation state needs

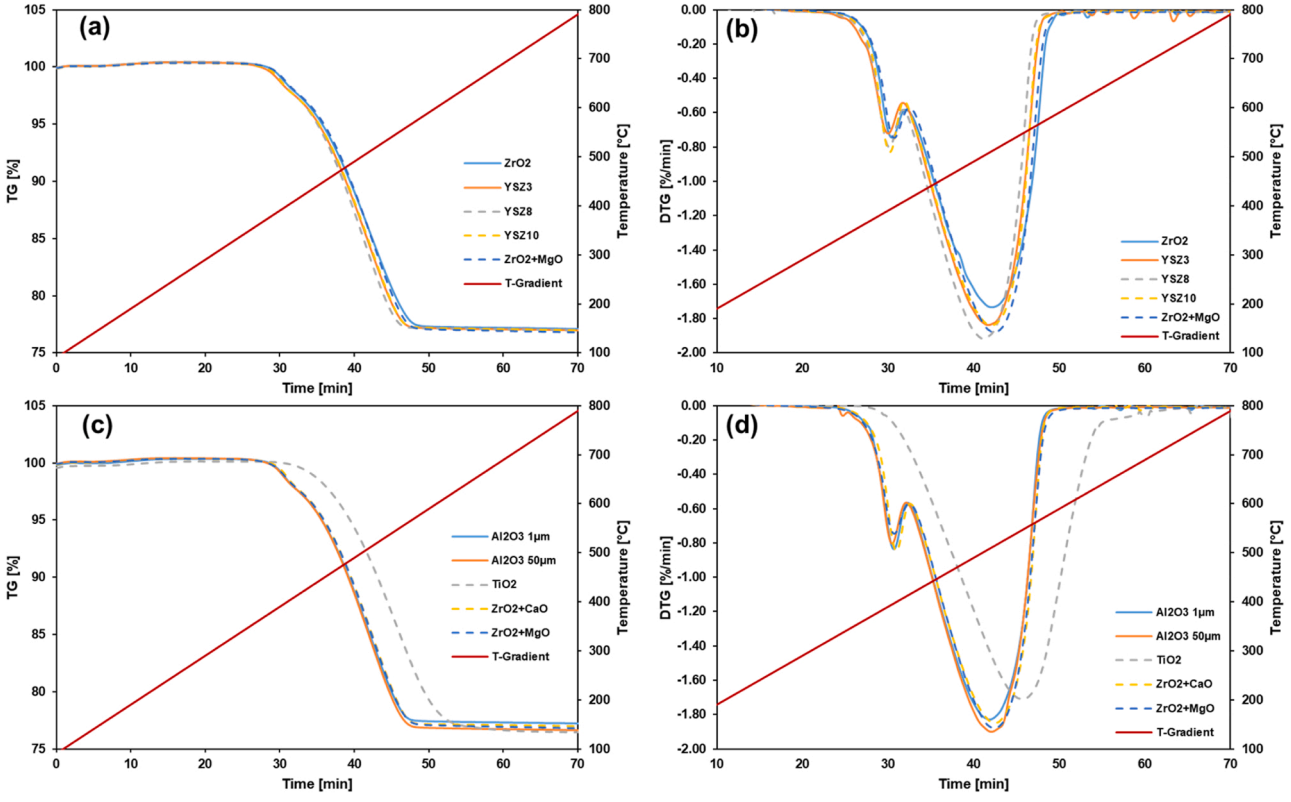

Fig. 4. TPR and DTG curve of the uncycled Fe_2O_3 samples with different support material in ratio the 80/20 wt.-%.

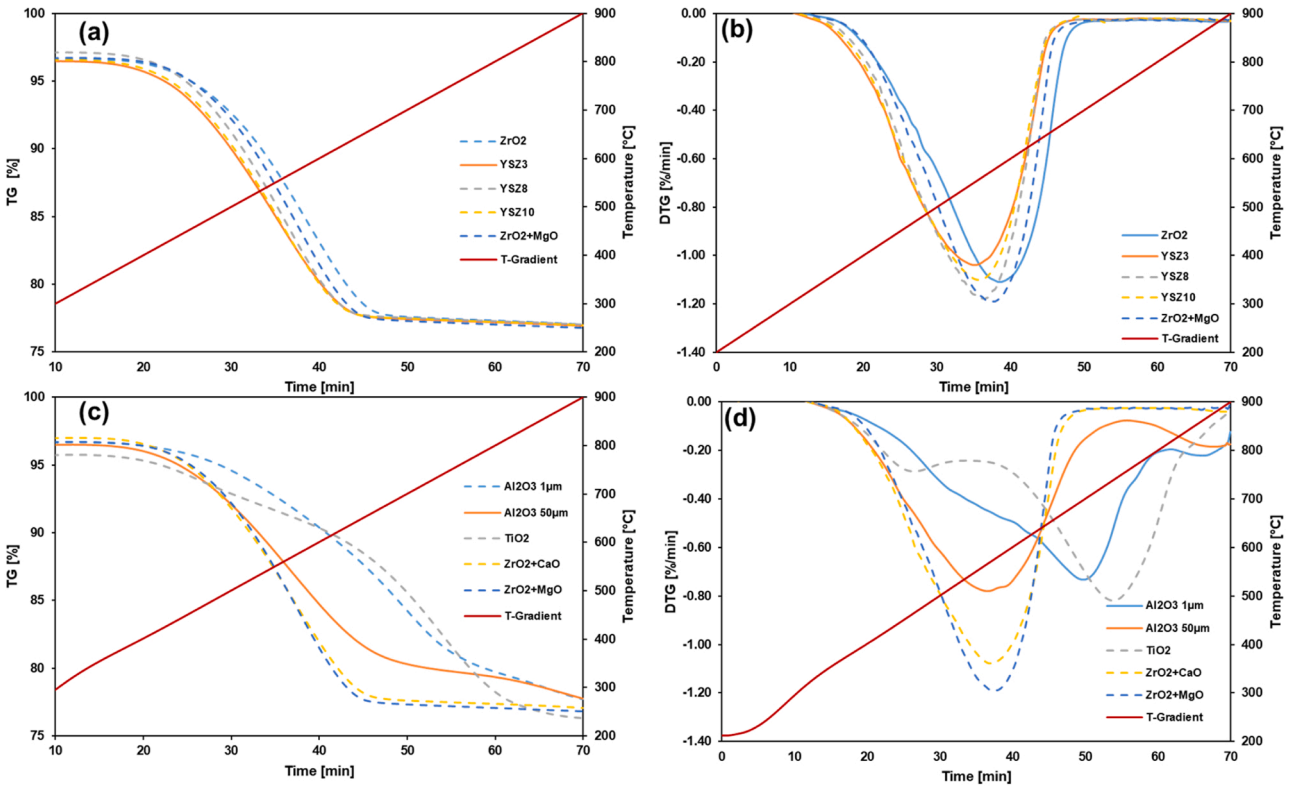

Fig. 5. TPR and DTG curve of the after 10 cyclisation steps of the Fe_2O_3 samples with different support material in ratio the 80/20 wt.-%.

higher energy for the reduction reaction. The broad peaks belong to the two subsequent reductions reaction of Fe_3O_4 to FeO (wüsit) and FeO to Fe [41]. This reaction takes place at a higher temperature. No real influence of the support material on the reduction mechanism of Fe_2O_3 to Fe could be determined. All reactions show the same reaction velocity at cycle 1, with the exception of TiO_2. The small peak at a lower temperature is missing for the titanium-based sample.

After 10 cycles of reduction and oxidation, a different DTG curve is obtained (see Fig. 5). In Fig. 5(a) and (b) it can be seen only one peak for each material in the DTG curve is visible at around 550 °C. All samples show nearly the same reduction performance. The reduction peak of Fe_2O_3 at around 380 °C is missing, because Fe can be only oxidized to Fe_3O_4 with water. Therefore, only the reduction of Fe_3O_4 to FeO and the subsequent reduction reaction to Fe takes during the reduction place. No formation of a reduction inhibiting side compound could be detected. This also applies for the sample with ZrO_2 +CaO as support material (see Fig. 5(c) and (d)). In chapter 3.2 a decreased reduction performance was detected by doping with CaO. The TPR analysis indicate that the phenomena belongs not to a side phase formation. A detailed explanation will be shown in the following chapter with the XRD and SEM analysis. Nevertheless, the comparison of the Fig. 5(a) and (b) with the samples in Fig. 5(c) and (d) showing different DTG curves were found for alumina and titanium stabilized samples compared to the ZrO_2 samples. Additional peaks were found at higher temperatures. Al_2O_3 with 50 µm shows a large peak at around 550 °C as in group one and an additional smaller peak shifted to 850 °C. The larger peak of Al_2O_3 with 1 µm particle size show, that the larger peak is shifted around 700 °C and also a small peak at 850 °C. Also TiO_2 show a twisted behavior, with a small peak at 500 °C and the bigger part of the reduction is taking place at higher temperature around 750 °C. The comparison of the TGA and DTG matches with the results of the performance of chapter 3.1 indicate a formation of an additional compound during the cyclisation is responsible for the decreased performance.

3.4. XRD analysis of cycled oxygen carrier

In this study, all samples were characterized by XRD after 10 cyclization steps in the reduced form. The corresponding characterizations are shown in Fig. 6. Pure cubic crystallized iron was found in all samples. No unreacted iron compound during the reduction of iron oxide such as FeO or Fe_3O_4 could be identified.

This indicates that the incomplete reduction of Al_2O_3 and TiO_2 –OC samples is not due to sintering, but probably to the formation of a non-reactive secondary phase. The formation of a secondary phase was not observed in any of the ZrO_2-based samples, which explains the high performance in reduction and oxidation. In addition, no chemical interaction of zirconia between the iron oxides and the support material was observed in the CaO-doped sample. This is consistent with the observations of the TPR analysis. Therefore, the decrease of SHP is due to a different phenomenon. In contrast, the material stabilized with TiO_2 and Al_2O_3 shows the formation of a minor phase. $FeAl_2O_4$ is detected in all Al_2O_3 samples, while a formation $Fe_{1.1}O_3Ti_{0.9}$ was found in TiO_2. This is consistent with the observation made in the literature that hercynite is found as an unreactive compound [27]. Thus, some of the iron is deactivated and is no longer available as active material. This explains the additional peaks in the TPR curves at 850 °C for the Al_2O_3 samples and TiO_2 and is also consistent with the decreasing values of SHP in Fig. 1. The use of ZrO_2 can prevent the reaction with the active ferrous material at high temperatures, and the performance of hydrogen storage and generation can be maintained over a series of cycles at high temperatures of 800 °C.

3.5. Morphological analysis of cycled oxygen carrier

In order to explain the phenomena of delayed oxidation performance, an examination of the surface morphology was also conducted using analysis SEM in addition to analyzing the chemical composition. Fig. 7 shows the morphology of the OCs after 10 cycles in the reduced state. It is clearly apparent here that a different crystal structure of the

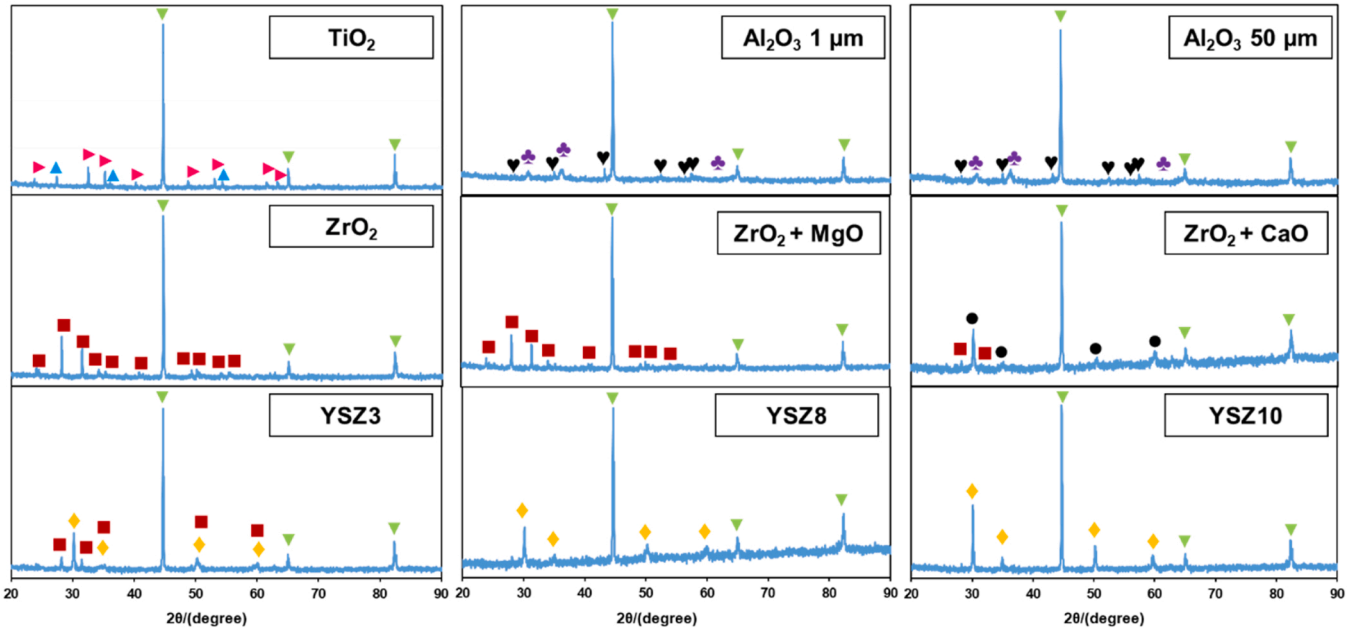

Fig. 6. XRD pattern of the OCs after 10 steps of cyclisation in the reduced state. (▼) Fe #52258-ICSD, (▶) TiO_2 (rutile) #33837-ICS, (▲) $Fe_{1.1}O_3Ti_{0.9}$ #23730-ICSD (♥)Al_2O_3 #10425-ICSD, (♣) $FeAl_2O_4$ #40093-ICSD, (■) ZrO_2_monclinic #41572-ICSD, (●) ZrO_2_cubic #89429-ICSD and (♦) Zirconium yttrium oxide _cubic #181236-ICSD.

respective support material is obtained during the cyclization. If the OC material stabilize the iron during the oxygen exchange and preventing the sintering phenomena, the iron is refined into small particles through oxidation and reduction [27,42]. The samples stabilized with pure ZrO_2 and those doped with yttrium and magnesia show a porous, homogeneously distributed surface with the formation of small crystals (Fig. 7 A-E). This explains the good performance over the number of cycles. The Al_2O_3 samples exhibit a porous morphology with the formation of small crystal structures on the surface. The drop in performance observed in the oxidation and reduction cycles is due to the formation of hercynite identified by XRD analysis. In the case of ZrO_2 + CaO (Fig. 7 F), a flatter and denser surface with larger grown crystals can be seen. Compared to doping the ZrO_2 with another alkaline earth metal such as MgO, no sintering of the surface is observed. The TiO_2 sample also shows a flat and denser morphology with non-small crystals on the surface. This explains the delayed oxidation performance and the low SHP for the samples stabilized with ZrO_2-CaO and titanium. For CaO, this is an important observation since the detected phenomena in the TGA could not be explained by TPR or XRD analysis. The decreasing reactivity is solely due to the change in morphology caused by the dopant. A denser and non-porous structure makes it difficult for the reactive gasses to penetrate into the iron/iron oxide matrix. These phenomena negatively affect hydrogen production and performance. In addition to preventing the formation of minor phases, additional highly porous surface formation with small and narrow crystal size distribution is beneficial for an efficient oxygen carrier, as shown for pure ZrO_2 and ZrO_2 stabilized with Y_2O_3 and MgO.

3.6. Cycling performance of the upscaled oxygen carrier in a fixed bed reactor system

Based on the small scale testing, the most promising oxygen carrier compositions were tested in a large-scale application. A detailed plan of the test facility and the parameters of the cycle process is displayed in Fig. 8. As a benchmark, the Fe_2O_3/Al_2O_3 80/20 wt.-% material was chosen from the work of Robert Zacharias et. al. for 100 cycles and 250 g of the respective OC with a pellet size distribution of 2–4 mm [27]. The SHP values were calculated from the data obtained. Additionally, the relative SHP in % to the benchmark was calculated for each sample and compared to the performance over the number of cycles. The experimental results are shown in Fig. 9a-e. It was found, that the TGA results differ significantly from the results in the small-scale application for the samples ZrO_2, ZrO_2 +MgO and YSZ3. The support material ZrO_2 and ZrO_2 +MgO show the lowest performance to the benchmark up to − 39% after a higher number of cycles. The oxygen exchange capacity of the iron oxide stabilized with ZrO_2 decreases sharply after the first cycle. Doping the ZrO_2 with MgO leads to an increased performance for the first few cycles. After 10 cycles, the performance is lower than the benchmark. Due to the inferior performance of the cyclisation with an upcoming pressure drop the experiments were canceled in the range of 30 cycles. The yttrium stabilized sample show a different behavior. The YSZ3 shows a high hydrogen production for the first 30 cycles. On increasing the number of cycles, the martial performance gradually decreases over the time of cyclisation and approaches the performance of Al_2O_3. The supporting materials with higher yttrium content such as YSZ8 and YSZ10 show an excellent performance over 100 cycles. The SHP is for the first 50 cycles, 10% higher for YSZ10 and for YSZ8 20%. At cycle 50 where the performance of benchmarked material decreases gradually, the yttrium-doped material keeps the oxygen exchange capacity stable. An increase improving of around 25–30% for YSZ10 and 35–40% for YSZ8 in hydrogen production and storage is achieved.

After cooling down the reactor, different pellets deformation observations were made after the cyclization regarding to the support material (see Fig. 9f). The YSZ 8 and YSZ 10 samples showed a partly sintered surface but the pellets structure was still intact. Whereas, the ZrO_2, ZrO_2 +MgO and YSZ3 showed a strong deformed material. Especially, YSZ3 was an almost powdery heavily collapsed contact mass. It has been accepted so far in the literature, that the cycling performance and stability of the pellets of the OC are only based on sintering or formation of a secondary phase [27]. However, these phenomena do not explain the difference of the material behavior in large scale for the ZrO_2 based materials, since no side formation appears as in Al_2O_3. All OCs show excellent oxidation and reduction performance, chemical inertness and porous and homogenous surface morphology in small scale. Therefore,

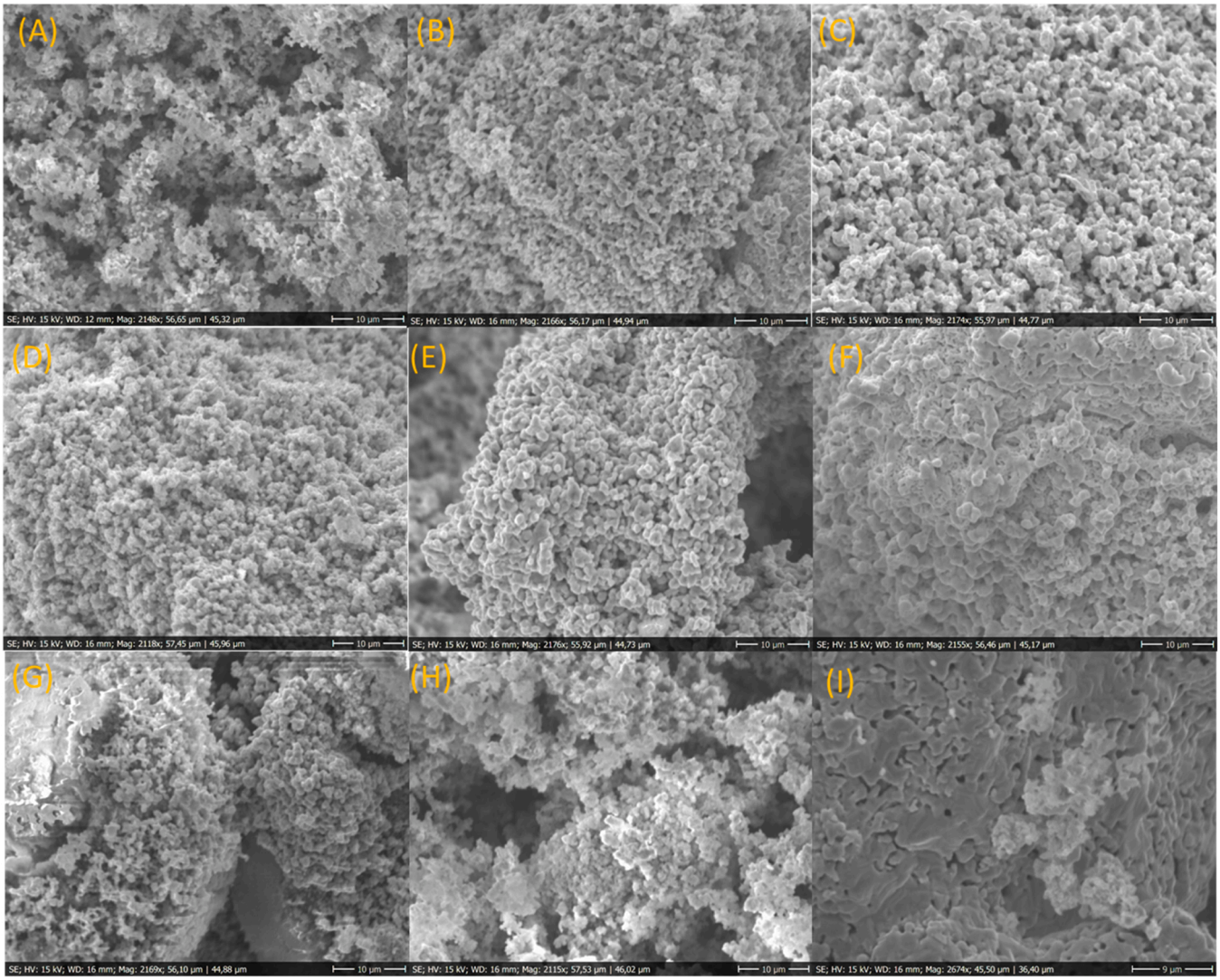

Fig. 7. SEM images of oxygen carrier samples with the compositions of 80 wt% Fe_2O_3 + 20 wt% of a respective support material: (A) ZrO_2, (B) YSZ3 (C) YSZ8 (D) YSZ10 (E) ZrO_2 +MgO (F) ZrO_2 +CaO (G) Al_2O_3 50 µm (H) Al_2O_3 1 µm (I) TiO_2.

additional phenomena must also play an important role in the CL hydrogen process, for the different performance in the reactor. In our process, due to the strong exothermic reaction during oxidation with water, temperatures of over 1000 °C were determined and a decrease to 740 °C was determined at the thermocouple in the endothermic reduction. All of this shows that the material is exposed to strong temperature influence. This indicates that not only the chemical inertness to the active material and the low sintering behavior of a supporting material are ideal for stabilizing the OC in large scale. Other factors such as microscopic phenomena must also play an important role in the CL hydrogen process, which have not yet been described in the literature of CL. For this purpose, HT-XRD, DSC, SEM/EDX and additional XRD characterization was carried out in order to uncover and understand the phenomena in the reactor.

3.7. *In situ time- resolved HT-XRD investigations*

The in situ investigations HT-XRD were carried out to elucidate the phenomenon of crystallographic phase changes occurring between the iron oxide and the support material during chemical looping hydrogen process in the reactor. Fe_3O_4 with support material were prepared out of the starting compounds by using the TGA set up. The HT-XRD measurements were performed at 800 °C, first in Ar atmosphere (0 min). Thereafter a gas composition of Ar/H_2 (5%) was added to the XRD reactor chamber and the change in crystal structure during the reduction of the compounds was studied. The first measurement was taken at 11 min until 145 min. The best performing material YSZ8 in the reactors can be seen as an example in Fig. 10. The course of the reaction of the other samples can be seen in the support information (Fig. S2-Fig.S5).

For the first measurement in Ar atmosphere, the diffractograms of all five samples show clear peaks associated with the cubic Fe_3O_4 at angles $2\theta = 29.9°$ (220), 35.2° (311), 36.9° (222), 42.8° (400), 53.1° (422), 56.6° (511), and 62.2° (440) (PDF 04–009–8443). The additional diffraction peaks in the first measurements belong to different support materials. In the case of ZrO_2 and ZrO_2 +MgO to monoclinic ZrO_2 at angles $2\theta = 28.2°$ (111), 31.5° (−111), 34.2° (002), and 50.1° (220) (01–086–1450) (Fig. S2 and S3). In the case of YSZ3 and YSZ8 to tetragonal yttrium zirconium oxide with angles $2\theta = 30.2°$ (101), 35.1° (110), 50.2° (112), 50.6° (200), 59.4° (103), and 60.0° (211) (PDF 04–016–2109) (Figs. S4 and 10). In the case of YSZ10 to cubic yttrium zirconium oxide at angles of $2\theta = 30.1$ (111), 34.9° (200), 50.1° (220), and 59.6° (311) (PDF 04–015–2373) (Fig. S5).

During the reduction in the Ar/H_2 atmosphere at 800 °C, the diffraction peaks belonging to the different support materials did not change, confirming that the crystal structure of the support materials is stable. Cubic Fe_3O_4 is first converted into cubic FeO during the

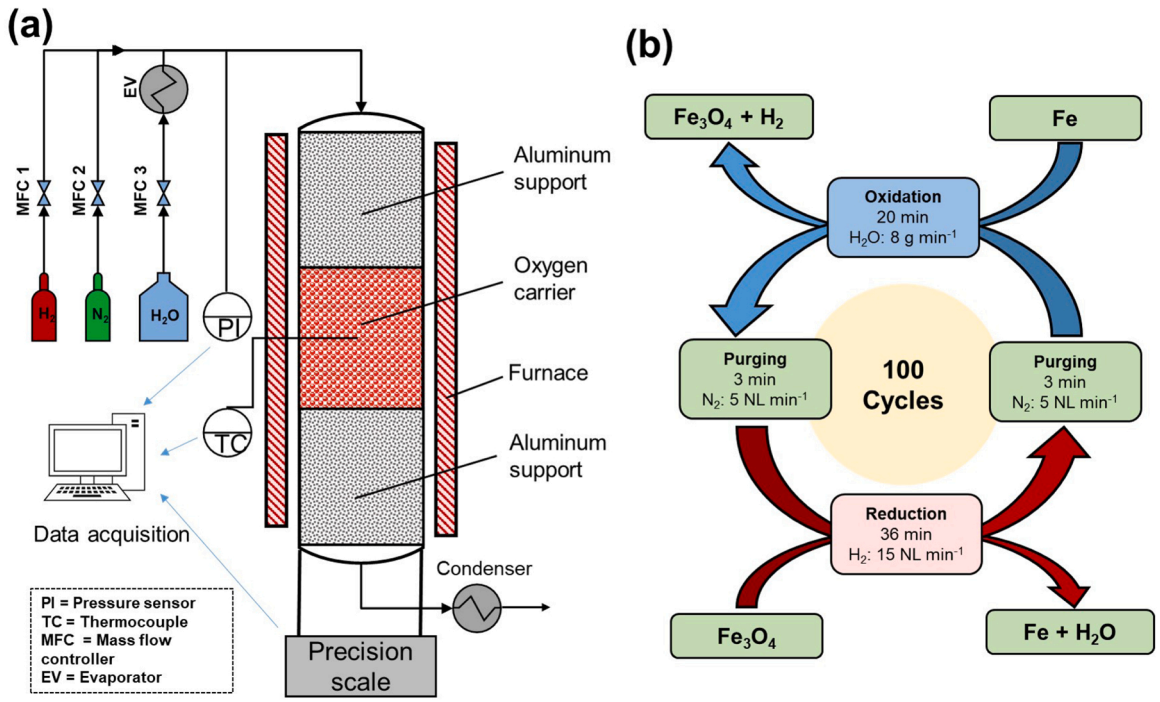

Fig. 8. Left: Fixed bed reactor setup for the gravimetric determination of the SHP of pelletized oxygen carrier samples. Right: Sequence of a cyclic in the fixed bed system for long-term determination of the SHP at 800 °C.

reduction, which is confirmed by the diffraction peaks at 2θ = 35.9° (111), 41.7° (200), 60.5° (220), and 72.4° (311) (PDF 01–089–2468) and then into cubic iron, which is confirmed by the diffraction peaks at angles 2θ = 44.4° (110), and 64.5° (200) (PDF 01–085–1410). The fastest reduction of Fe_3O_4 to iron occurs when the ZrO_2, YSZ3 and YSZ8 were used as supporting materials and the slowest when YSZ10 is used.

In Fig. 11 the crystal structures are visualized based on the HT-XRD-data. During the reduction the unit cell of the iron compound shrinks from Fe_3O_4 with cell length of a = b = c = 4.3 Å, to cubic iron with the dimension of 2.88 Å. Due to the reaction of hydrogen with the bonded oxygen (red) at the iron crystal lattice (gold), releasing water the crystal lattice gradually shrinks in the reactor. The in situ XRD investigations show that the unit cell a = b = c decreases evenly during the reduction cycle and the angles of the unit cell remain the same. Comparing the HT-XRD data with cycling performance of the upscale OC in a fixed bed reactor system, a connection between the lattice mismatch of the support material and hydrogen production performance is evident. This indicates that when oxygen is exchanged in the iron lattice, a stress in the material arises, as in pure ZrO_2 or doped with MgO support material where a monoclinic unit cell is detected during the reduction. In Fig. 11 b can be seen that the zirconium lattice deviated from the cell geometry of the cubic iron. The monoclinic cell has three different axis lengths where a = 5.15010 b = 5.20770 c= 5.31710 and the angel is α = γ = 90° β = 99.224°. The tilt of the c axis introduce additional an unfavorable geometry for the active iron material. Hence, a lattice mismatch is created which destabilize the pellet stability. This increase the probability of a fracture and explain the performance in the reactor. On the other hand using Y_2O_3 as the doping agent (Fig. 11 c) changes the geometry of the unit cell and leads to a cubic/tetragonal ZrO_2. The cubic/tetragonal crystal structure of the support material match with geometry of the iron compounds and has a stabilizing effect. The YSZ material minimize the lattice mismatch. The distribution of support material is intended to prevent the iron from sintering during cycling. By using support material with the same chemical behavior (inert during cyclization), the microscopic phenomena such as the same crystal structure as that of the active material play an important role. Therefore, pellet breakage and deformation can be minimized and suppressed.

3.8. Determination of the crystal structure change of the support material

Based on the result of the in situ HT-XRD and the pellet stability in the large-scale application the support materials were examined with DSC to investigate if an additional microscopic phenomenon appears, such as a change in the crystal structure and underline the observation. The pure support materials were heated up to 1200 °C and cooled down with 15 K/min, to simulate the reduction behavior in the reactor during oxidation and reduction. The results are shown in Fig. 12. The pure support material ZrO_2, ZrO_2 +MgO and YSZ 3 show an exothermic peak, which is a signal for the change in the crystal structure (see Fig. 12). For pure Al_2O_3, YSZ8 and YSZ10 no peak in the DSC analysis was detected. This is in agreement with the literature, where the addition of higher yttrium content stabilizes the cubic phase of ZrO_2 and suppress the phase transformation into tetragonal or monoclinic structure at higher temperature [40]. The peak for ZrO_2 appears at 899 °C. In the literature, a phase-transition mechanism of from tetragonal to monoclinic ZrO_2 is noted at this temperature region for pure zirconium oxide [40]. The peak for ZrO_2 +MgO is shifted to lower temperature at 793 °C. Doping ZrO_2 with a small quantity of yttrium shows a peak at around 1150 °C for pure YSZ3. This is consistent with XRD studies in the literature where partially stabilized YSZ starts decomposing into two phases at temperatures from 1100° to 1300°C [43]. The low yttrium content transform the tetragonal YSZ slowly into a monoclinic polymorph structure during the oxidation. Comparing the DSC results with the reactor temperature in large-scale testing shows that the phase change for the pure ZrO_2 support material is in the temperature range in which the oxidation and reduction occurs. A component, which is cooled through the transformation temperature, becomes heavily micro cracked and therefore crumbles [44]. Doping with MgO decreases the peak to a lower temperature, which is only reached in the reduction cycle. In comparison to pure ZrO_2, a doped ZrO_2 with MgO shows in the first 10 cycles, an increase to the benchmark material can be achieved. A slight progressive degradation of the structure takes place after the 10 cycles due to the change in crystallization (see Fig. 9d and e). In Fig. 13 the microscopic phenomena is visualizes the deformations of the support material. The figures show the change of the cell geometry during the cooling at the

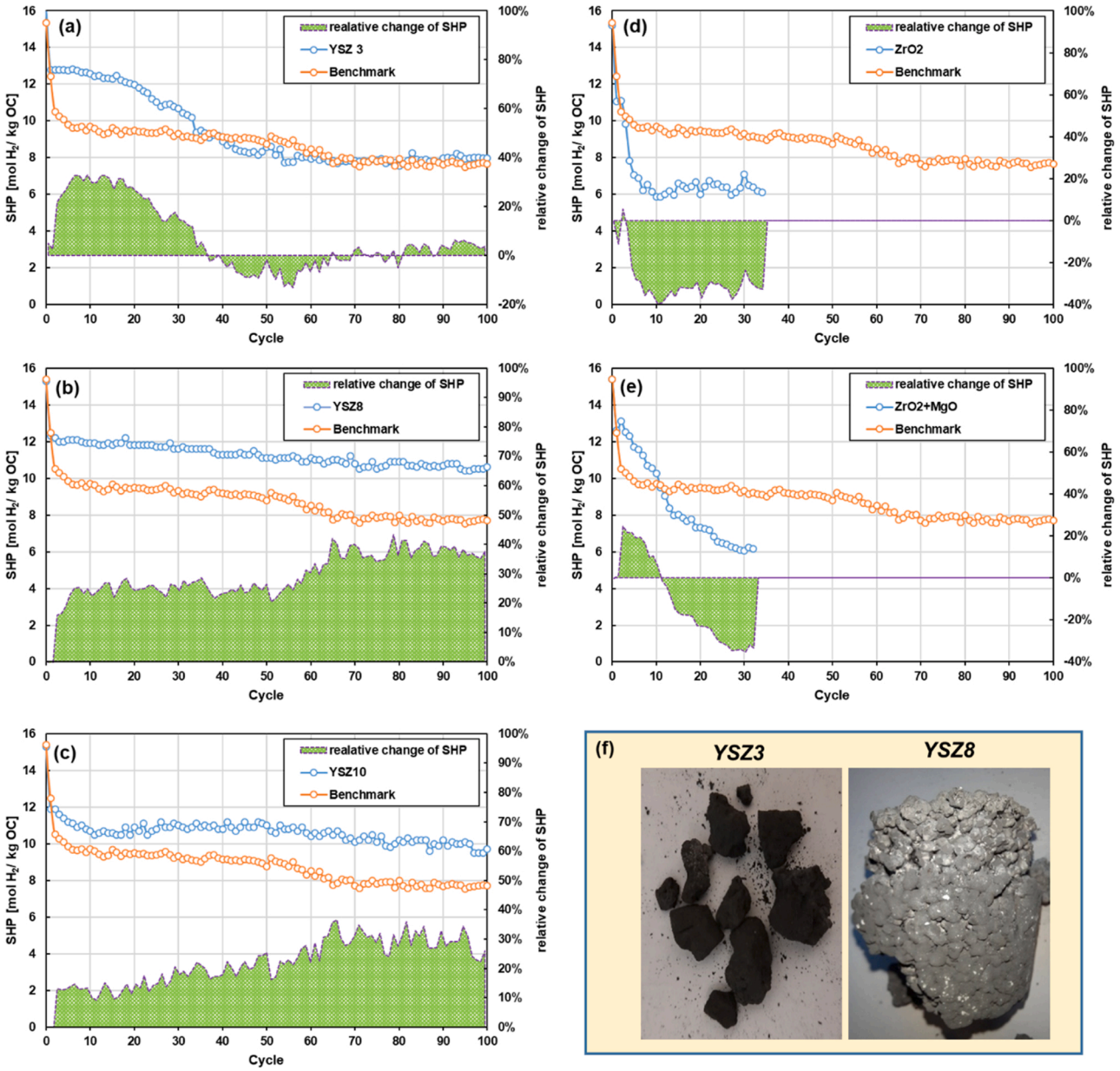

Fig. 9. Long-term cycle experiment in a fixed-bed reactor over 100 cycle (a-e). The specific hydrogen production results of the oxygen carrier pellets with the following compositions of 80 wt.-% Fe_2O_3 + 20 wt.-% (blue line) to the respective support material: (a) YSZ3, (b) YSZ8, (c) YSZ10, (d) ZrO_2 and (e) ZrO_2 +MgO. The benchmark 80 wt.-% Fe_2O_3 + 20 wt.-% Al_2O_3 (orange line) is plotted relative to the change in % of SHP (green area). (f) Pellets after 100 cycle in reduced form; left Fe-YSZ3 and right Fe-YSZ8.

reduction and the heating at the oxidation cycle of the material. The change between the tetragonal and monoclinic unit cell lead to an overall volume change in the unit cell about 4% for ZrO_2 [44,45]. Changes in the cell parameters such as edge length and angle have in consequence a larger lattice mismatch of the unit cell to the active material. Therefore, a deformation occurs in the OC, which is accompanied by a resulting stress in the material itself. In comparison to the DSC and XRD results it is shown, that Al_2O_3 show a formation of the side phase hercynite, which decrease the oxidation and reduction performance in small scale. However, the DSC show no change of the crystal structure of the aluminum support material itself, which explain the pellets stability for large-scale application compared to pure ZrO_2 and ZrO_2 +MgO as supporting material for stabilizing the active material.

Nevertheless, for YSZ3 the much slower and more gradual decrease in the specific hydrogen production performance could not really be explained with DSC analysis compared to pure ZrO_2 and ZrO_2 +MgO (see Fig. 9). Since the phase, transition is outside the temperature range in the reactor, the YSZ3 should perform similar to YSZ8 and YSZ 10. Compared to all other samples YSZ3 show a mixture in the crystal structure of the tested support material in small scale (see Fig. 6), whereas YSZ8 and YSZ10 stay cubic after 10 cycles in the TGA experiment. The idea was thus investigated of whether a phase change due to the exposure to water vapor or hydrogen occurs and is responsible for the different behavior to YSZ8 and YSZ10 in the reactor. It has been observed in the literature that a tetragonal to monoclinic transformation can take place with water vapor in the case of partially stabilized YSZ [46]. Therefore, the pure YSZ3 was cycled at 800 °C without any addition of iron for 20 cycles. No change of the mass was detected during oxidation and reduction cycle in the TGA. The results are shown in Fig. 14. The XRD study show a significant change of the crystal structure of the YSZ3 is detected due to the exposed to water vapor and hydrogen. The volumetric composition was calculated with the Rietveld

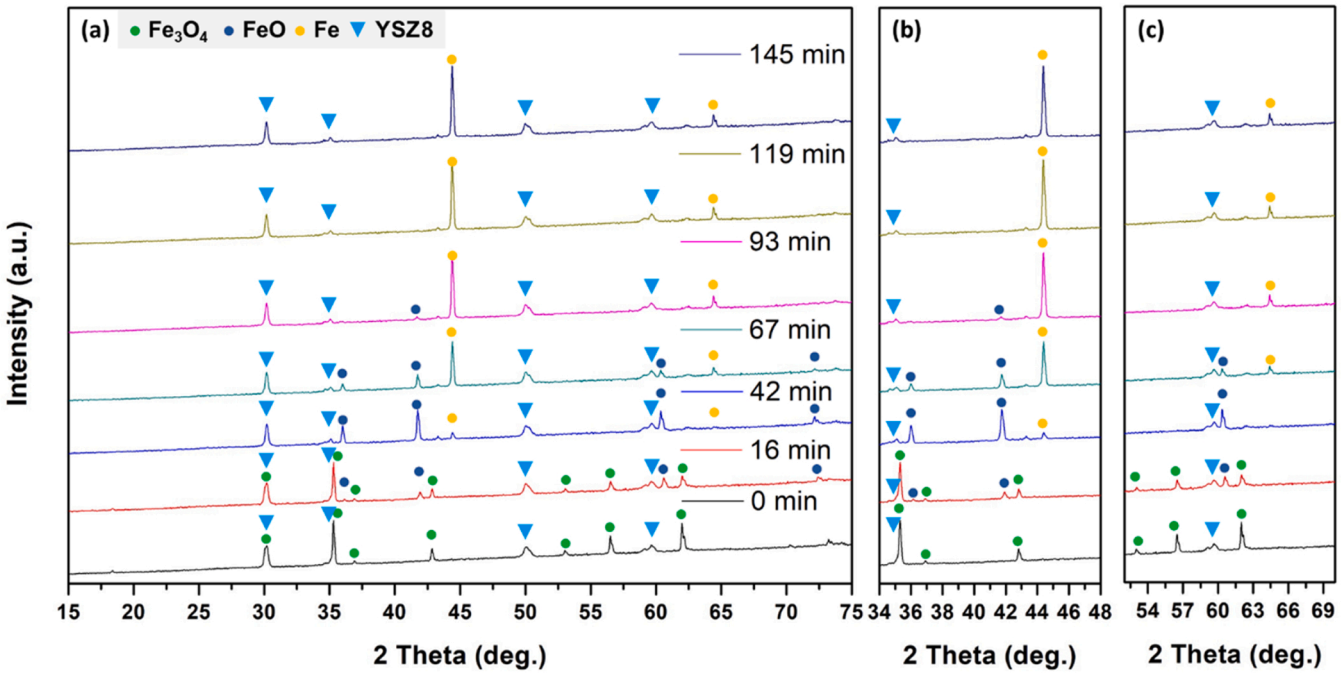

Fig. 10. High-temperature X-ray diffraction (HT-XRD) patterns at 800 °C in Ar atmosphere at 0 min and in Ar atmosphere containing 5 vol% H_2 at 16–145 min of the oxygen carrier samples 80 wt% Fe_3O_4 + 20 wt%YSZ8. (a) full spectra and (b) + (c) zoom spectra.

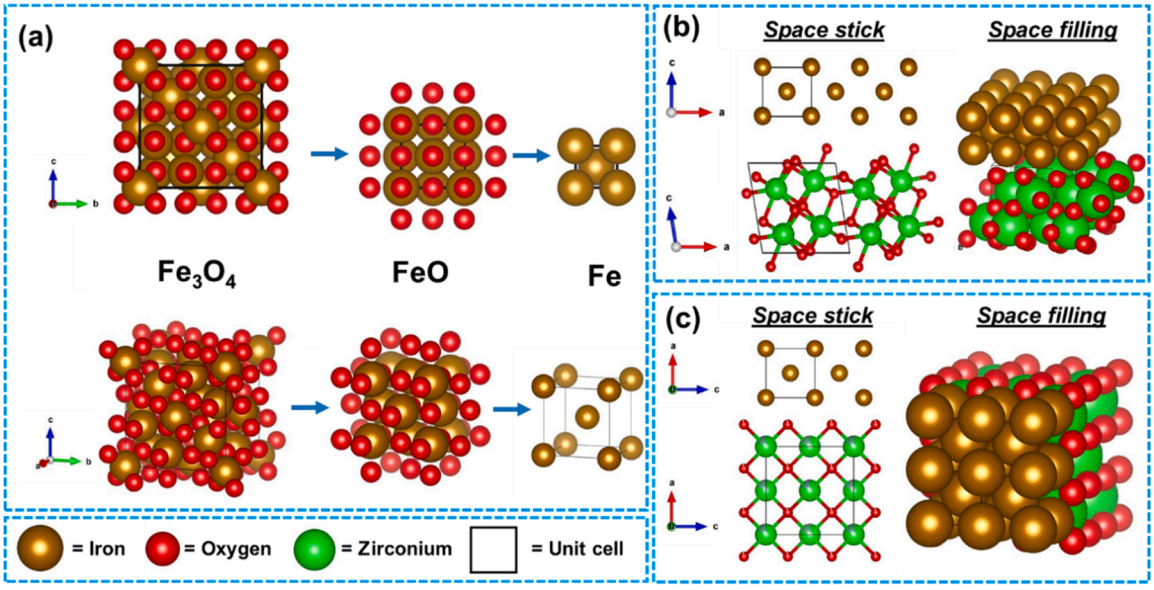

Fig. 11. Representation of the crystal structure (a) Change of the unit cell of Fe_3O_4 into FeO and Fe during the reduction. (b) Heterogenic composition of cubic-Fe with monoclinic ZrO_2 unit cell (c) Heterogenic composition of cubic-Fe with cubic-ZrO_2 unit cell based on doping with Y_2O_3.

refinement from the spectra. The ratio of the composition from Fig. 6 YSZ3 was also calculated for the support material. The quantitative phase analysis is shown in Table 1. The results show a gradual change in the crystal structure from cubic/monocline (a distinction between cubic or monoclinic ZrO_2 cannot be determined due to the complete overlapping of the reflections) into a tetragonal phase changes with the number of the cyclisation. The slow and gradual phase change of the support material at 800 °C itself explains the pulverization of the pellet, which was observed in Fig. 9(f). From the previously discussed results, it is clear that a monoclinic-to-tetragonal transformation causes a volume change in the unit cell. The change of the microscopic phenomena results in the change of the macroscopic level and results in cracking and material failure. For this reason, a monoclinic phase in ZrO_2 support material for CL hydrogen production in fixed-bed systems should avoided. In addition, a full stabilization of the cubic-ZrO_2 oxide with Y_2O_3 is needed to avoid phase transformation due partial stabilized unit cell in case of YSZ3.

3.9. *The effect of agglomeration on the sintering performance*

A last difference that still had to be clarified is the better behavior of YSZ8 compared to YSZ 10. The TGA characterization showed no deviation whatsoever with regard to oxygen and reduction as well as cyclic stability. The microscopic analysis by means of DSC and in situ HT-XRD

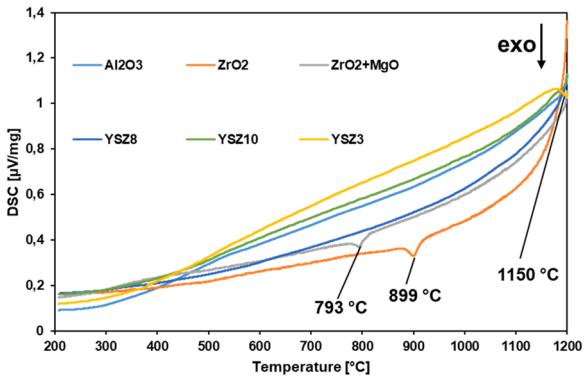

Fig. 12. DSC cooling curve of the pure support material.

also shows no chemical and physical difference, which can explain the phenomena in large scale.

Therefore, an SEM analysis in combination using also an EDX mapping was performed to see if a difference in homogeneity could explain the slightly better behavior of YSZ8 than YSZ10. As compound, the starting material of the in situ HT-XRD analysis was used. In Fig. 15 the mapping results are shown. In the SEM image of Fig. 15 1a) and 2a) brighter spots can be seen, which indicate a poorly conductive material. The EDX analysis clearly shows that these points are an agglomeration of the support material yttrium stabilized zirconium oxide. For the EDX analysis of the darker spots shows that the matrix is mostly iron oxide. A closer look on the elemental composition of 1d) and 2d), which belongs to the dark spots, shows that a different quantity of support material is found in the iron rich region. A detail characterization of the elemental composition of the dark spots show, in the YSZ8 sample (Fig. 15 1d) a mass composition of 12.3 wt.-% Zr is analyzed, whereas YSZ10 only 4.1 wt.-% Zr is found (Fig. 15 2d). This shows that the YSZ8 spreads better when making the pellets with the iron due to the small particle size. Thereby a decrease of the formation of agglomeration island of supporting material is achieved. Comparing the SEM images of YSZ8 and YSZ10 results in better material homogeneity for YSZ8 in pellet manufacturing (Fig. 15 1a and 2a). Thus, greater spatial separation of the iron is achieved during cyclization. Therefore, sintering of the iron can be minimized. This allows a higher specific hydrogen production performance in case of YSZ8 and YSZ 10, if comparable properties like chemical reactivity (inertness to the iron) and similar crystal phases. The EDX mapping for the OC composition of ZrO_2, ZrO_2 +MgO and YSZ3 are shown in Fig. S6. No recognizable connection with the SEM/EDX analysis on the large scale results can be found. The effects are therefore based exclusively on the microscopic effect of the phase change of the unit cell. The investigation shows once again that despite approaching homogeneity, chemical underactivity and morphological properties, the microscopic phenomenon of crystal phase change is the most important point of the successful scale up.

4. Conclusions

In the present work, a broad material screening was performed in the range of Al_2O_3, TiO_2 and ZrO_2 support materials. It was found that the zirconia material yielded the highest specific hydrogen production (SHP) above 12.5 mmol H_2/gOC compared to the literature. Detailed material studies revealed that support materials based on Al_2O_3 and TiO_2 lead to a significant decrease in SHP, which is due to the formation of a non-reactive side compound with the active iron detected by XRD. When ZrO_2 is used the reduction and oxidation are higher due to its chemical inertness towards the active iron. In addition, zirconia exhibits an excellent surface morphology. Differences were found in the influence of ZrO_2 doping. The dopants Y_2O_3 and MgO have a positive influence, while CaO decreases the performance. The phenomenon of

Table 1
Calculated volume ratio of the crystal structure change of pure YSZ3 uncycled, 10 times and 20 times cycled.

Sample	Monoclinic/cubic [%]	Tetragonal [%]
pure YSZ 3	50	50
10 x cycled YSZ 3	36	64
20 x cycled pure YSZ 3	8	92

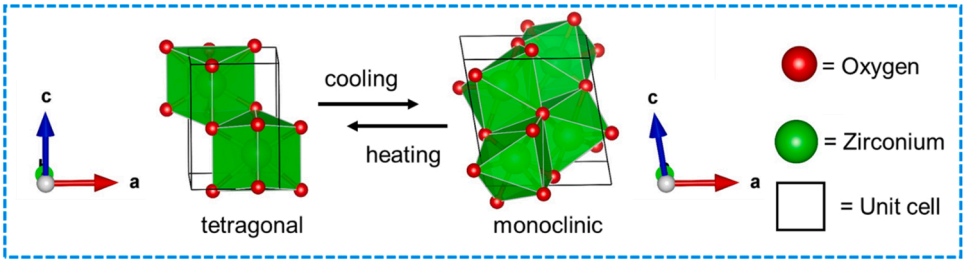

Fig. 13. Schematic representation of the polymorphic transformation during cooling/heating of ZrO_2 of the space group tetragonal (T) and monoclinic (M) (from left to right).

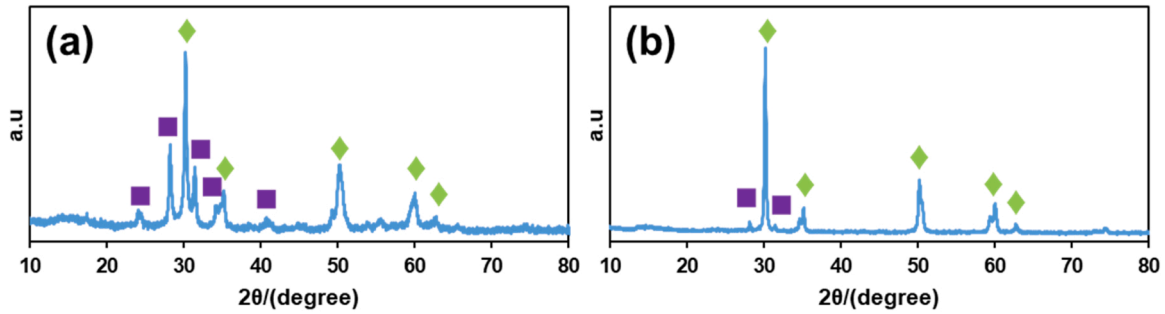

Fig. 14. XRD pattern of pure YSZ 3 (a) uncycled and (b) after 20 cycles steps. (■) Baddeleyite #96537-ICSD or Zirconium yttrium oxide _cubic #181236-ICSD (♦) Zirconium yttrium oxide #86603-ICSD.

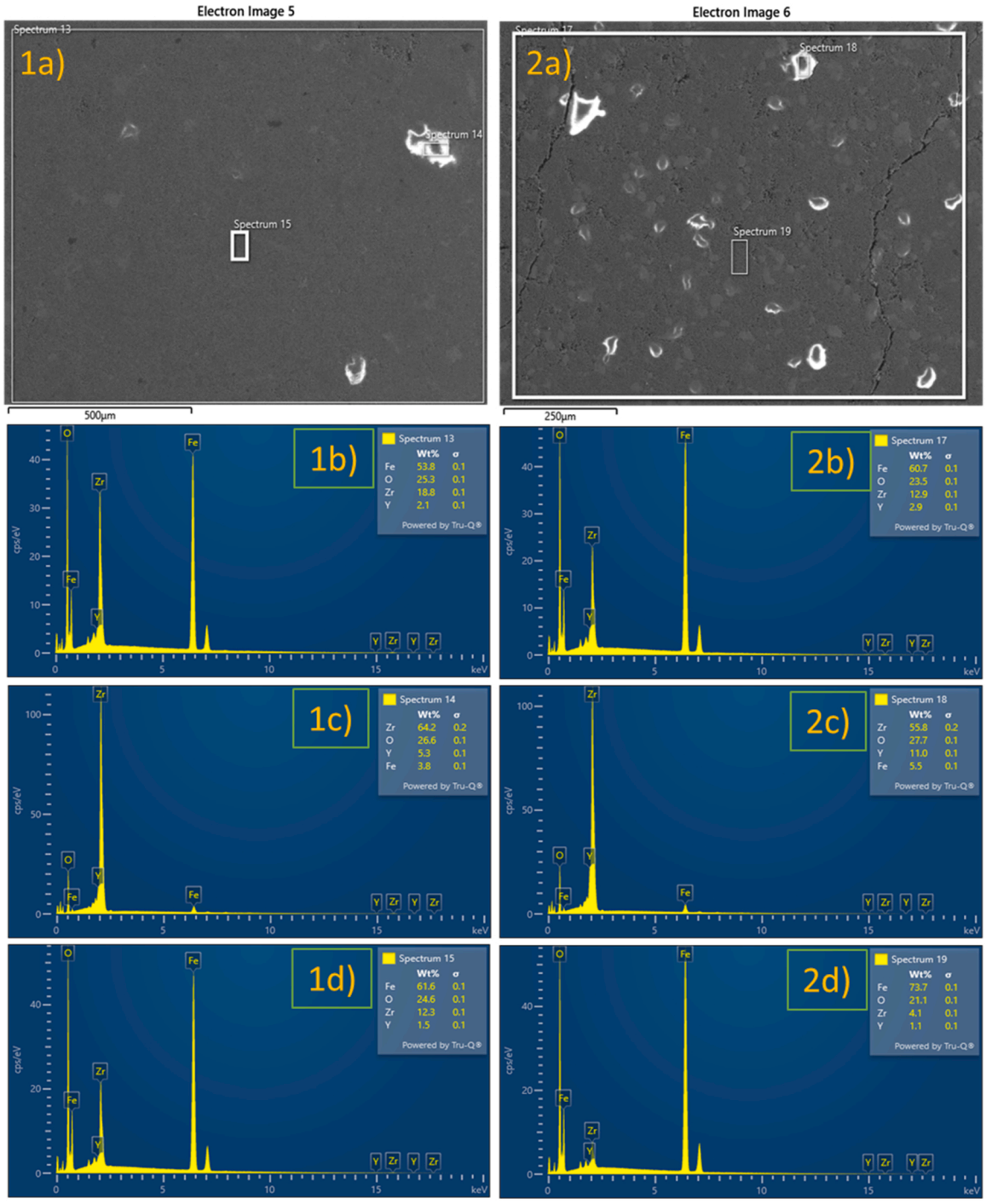

Fig. 15. 1a) SEM Image of Fe_3O_4 stabilized with YSZ8 in the ratio 80/20 wt.-%. 1b-d) EDX spectra of the different spots in 1a). 2a) SEM Image of Fe_3O_4 stabilized with YSZ10 in the ratio 80/20 wt.-%. 2b-d) EDX spectra of the different spots in 2a).

doping ZrO_2 with another alkaline earth shows that MgO leads to the formation of small iron crystals. Calcium, on the other hand, sintered the surface of the oxygen carrier (OC). The release of hydrogen with water vapor is thus hindered in ZrO_2 +CaO stabilized materials. Based on the experimental results, the promising candidates were tested in large-scale applications.

Three material compositions were found (YSZ3, YSZ8 and YSZ10) to exceed the benchmark value of up to 40% molH_2/kg OC in large-scale applications as reported in the literature. The study clearly shows that it is not only the chemical inertness or the morphology that is the bottleneck for a suitable upscaling, as assumed in the literature. A support material has also to stabilize the Fe_3O_4/Fe in the reactor. Based on HT-XRD and DSC characterization it was shown that the microscopic phenomena play a key role in pellet stability and hydrogen production. The matching of the crystal phases to the cubic structure of the active material is essential for the successful operation of a large-scale fix-bed reactor. A monoclinic to tetragonal phase transition of the support material leads to pulverization and pressure drop in the reactor. This process can be delayed by shifting the phase transition to a lower temperature by doping zirconia with MgO. Although Al_2O_3 reacts with iron to form an unreactive $FeAl_2O_4$, the cyclic stability was higher than the chemically inert pure ZrO_2 and ZrO_2 doped with MgO material. The

Al_2O_3 show no phase change in the DSC, which results in significantly higher SHP in the reactor. This shows that microscopic phenomena, especially the change of unit cell geometries of the material, have the most fundamental influence on the production and storage capacity of hydrogen in the CL process. To enable long-term stable operation of the CL hydrogen process, a cubic/tetragonal phase is required for high values in large-scale hydrogen production. Doping ZrO_2 with Y_2O_3 at higher concentration stabilizes the pellet structure in the reactor and shows excellent behavior due to suppression of phase transformation. Low concentrations of Y_2O_3 in the range of 3% cause a gradual change in the unit cell ratio from cubic/monoclinic to tetragonal due to the contact with the steam and hydrogen environment in the reactor. Therefore, monoclinic/tetragonal phase transformation in the ZrO_2 support material has to be completely avoided due to the lattice mismatch for CL hydrogen production in fixed bed systems. Doping with a higher Y_2O_3 concentration shows no visible phase transition and therefore has stable performance over 100 cycles. In summary, YSZ 8 and YSZ10 has been demonstrated to produce hydrogen production above 10 molH_2/kgOC on a 250 g scale over 100cycles for fixed bed chemical looping systems. Additional homogeneity in the pellets enhance the SHP per cycle. Using SEM /EDX, the YSZ8 demonstrated to provide better distribution in the iron matrix and better separation during reduction and oxidation. The work demonstrates the importance of microscopic phenomena and brings a new approach to OC design for implementing it in a large-scale system. The pre-selection in material screening with respect to scale-up in chemical looping technology will need to be considered in future. Therefore, new suitable support materials should be developed in terms not only of chemical inertness or good morphology to achieve successful upscaling. In addition, the crystal phases should match the active material and polymorphic transformations will play a fundamental role in stabilizing the Fe_3O_4/Fe active material in a fixed-bed chemical looping for efficient green hydrogen production.

CRediT authorship contribution statement

Fabio Blaschke: Proposed the research project, methodology, synthesis and material testing small and large scale, Characterization and Data interpretation, visualization Writing – original draft, **Marjan Bele:** Methodology, Characterization and Data interpretation, Writing – review & editing, **Brigitte Bitschnau:** Characterization and Data interpretation, **Viktor Hacker:** Project administration, Supervision, Funding acquisition, Writing – review & editing.

Declaration of Competing Interest

The authors declare that they have no known competing financial interests or personal relationships that could have appeared to influence the work reported in this paper.

Data availability

Data will be made available on request.

Acknowledgements

Financial support by the Austrian Science Fund (FWF): P 34824 is gratefully acknowledged.

Appendix A. Supporting information

Supplementary data associated with this article can be found in the online version at doi:10.1016/j.apcatb.2023.122434.

References

[1] H.L. Chen, H.M. Lee, S.H. Chen, Y. Chao, M.B. Chang, Review of plasma catalysis on hydrocarbon reforming for hydrogen production-Interaction, integration, and prospects, Appl. Catal. B Environ. vol. 85 (1–2) (2008) 1–9, https://doi.org/10.1016/j.apcatb.2008.06.021.
[2] G.W. Crabtree, M.S. Dresselhaus, M.V. Buchanan, The hydrogen economy, Phys. Today vol. 57 (12) (2004) 39–44, https://doi.org/10.1063/1.1878333.
[3] Z. Li, M. Li, Z. Bian, Y. Kathiraser, S. Kawi, Design of highly stable and selective core/yolk-shell nanocatalysts-review, Appl. Catal. B Environ. vol. 188 (2016) 324–341, https://doi.org/10.1016/j.apcatb.2016.01.067.
[4] A. Midilli, M. Ay, I. Dincer, M.A. Rosen, On hydrogen and hydrogen energy strategies, I: Curr. Status needs," *Renew. Sustain. Energy Rev.* vol. 9 (3) (2005) 255–271, https://doi.org/10.1016/j.rser.2004.05.003.
[5] Global Hydrogen Review 2021, Glob. Hydrog. Rev. (2021) *2021*, https://doi.org/10.1787/39351842-en.
[6] O.A. Omoniyi, V. Dupont, Optimised cycling stability of sorption enhanced chemical looping steam reforming of acetic acid in a packed bed reactor, Appl. Catal. B Environ. vol. 242 (August 2018) (2019) 397–409, https://doi.org/10.1016/j.apcatb.2018.09.083.
[7] J.D. Holladay, J. Hu, D.L. King, Y. Wang, An overview of hydrogen production technologies, Catal. Today vol. 139 (4) (2009) 244–260, https://doi.org/10.1016/j.cattod.2008.08.039.
[8] International Energy Agency, "The Future of Hydrogen: Seizing today's opportunities," 2019. [Online]. Available: ⟨https://www.iea.org/reports/the-future-of-hydrogen⟩.
[9] J. Chi, H. Yu, Water electrolysis based on renewable energy for hydrogen production, Cuihua Xuebao/Chin. J. Catal. vol. 39 (3) (2018) 390–394, https://doi.org/10.1016/S1872-2067(17)62949-8.
[10] S. Fujiwara, et al., Hydrogen production by high temperature electrolysis with nuclear reactor, Prog. Nucl. Energy vol. 50 (2–6) (2008) 422–426, https://doi.org/10.1016/j.pnucene.2007.11.025.
[11] C. Acar, I. Dincer, Comparative assessment of hydrogen production methods from renewable and non-renewable sources, Int. J. Hydrog. Energy vol. 39 (1) (2014) 1–12, https://doi.org/10.1016/j.ijhydene.2013.10.060.
[12] A. Ursua, P. Sanchis, L.M. Gandia, Hydrogen production from water electrolysis: current status and future trends, Proc. IEEE vol. 100 (2) (2012) 410–426.
[13] C. Koroneos, A. Dompros, G. Roumbas, N. Moussiopoulos, Life cycle assessment of hydrogen fuel production processes, Int. J. Hydrog. Energy vol. 29 (14) (2004) 1443–1450, https://doi.org/10.1016/j.ijhydene.2004.01.016.
[14] P. Nikolaidis, A. Poullikkas, A comparative overview of hydrogen production processes, Renew. Sustain. Energy Rev. vol. 67 (2017) 597–611, https://doi.org/10.1016/j.rser.2016.09.044.
[15] S.Z. Zhiznin, S. Vassilev, A.L. Gusev, Economics of secondary renewable energy sources with hydrogen generation, Int. J. Hydrog. Energy vol. 44 (23) (2019) 11385–11393, https://doi.org/10.1016/j.ijhydene.2019.03.072.
[16] N. Armaroli, V. Balzani, The hydrogen issue, ChemSusChem vol. 4 (1) (2011) 21–36, https://doi.org/10.1002/cssc.201000182.
[17] G. Voitic, V. Hacker, Recent advancements in chemical looping water splitting for the production of hydrogen, RSC Adv. vol. 6 (100) (2016) 98267–98296, https://doi.org/10.1039/c6ra21180a.
[18] M. Luo, et al., Review of hydrogen production using chemical-looping technology, Renew. Sustain. Energy Rev. vol. 81 (July 2017) (2018) 3186–3214, https://doi.org/10.1016/j.rser.2017.07.007.
[19] T. Mendiara, et al., Negative CO_2 emissions through the use of biofuels in chemical looping technology: a review, Appl. Energy vol. 232 (April 2018) (2018) 657–684, https://doi.org/10.1016/j.apenergy.2018.09.201.
[20] N. Giannakeas, A. Lea-Langton, V. Dupont, M.V. Twigg, "ydrogen from scrap tyre oil via steam reforming and chemical looping in a packed bed reactor, Appl. Catal. B Environ. vol. 126 (Sep) (2012) 249–257, https://doi.org/10.1016/J.APCATB.2012.07.010.
[21] J. Hu, V.V. Galvita, H. Poelman, C. Detavernier, G.B. Marin, Catalyst-assisted chemical looping auto-thermal dry reforming: spatial structuring effects on process efficiency, Appl. Catal. B Environ. vol. 231 (. 2018) 123–136, https://doi.org/10.1016/J.APCATB.2018.03.004.
[22] S. Bock, R. Zacharias, V. Hacker, Experimental study on high-purity hydrogen generation from synthetic biogas in a 10 kW fixed-bed chemical looping system, RSC Adv. vol. 9 (41) (2019) 23686–23695, https://doi.org/10.1039/c9ra03123e.
[23] B. Stoppacher, T. Sterniczky, S. Bock, V. Hacker, On-site production of high-purity hydrogen from raw biogas with fixed-bed chemical looping, Energy Convers. Manag. vol. 268 (2022), 115971, https://doi.org/10.1016/J.ENCONMAN.2022.115971.
[24] Y. Kang, et al., Promoted methane conversion to syngas over Fe-based garnets via chemical looping, Appl. Catal. B Environ. vol. 278 (June) (2020), 119305, https://doi.org/10.1016/j.apcatb.2020.119305.
[25] Z. Yu, et al., Iron-based oxygen carriers in chemical looping conversions: a review, Carbon Resour. Convers. vol. 2 (1) (2019) 23–34, https://doi.org/10.1016/j.crcon.2018.11.004.
[26] Y. Zhu, et al., Bimetallic BaFe2MAl9O19 (M = Mn, Ni, and Co) hexaaluminates as oxygen carriers for chemical looping dry reforming of methane, Appl. Energy vol. 258 (2020), 114070, https://doi.org/10.1016/J.APENERGY.2019.114070.
[27] R. Zacharias, S. Bock, V. Hacker, The impact of manufacturing methods on the performance of pelletized, iron-based oxygen carriers for fixed bed chemical looping hydrogen in long term operation, Fuel Process. Technol. vol. 208 (March) (2020), 106487, https://doi.org/10.1016/j.fuproc.2020.106487.

[28] K.S. Kang, C.H. Kim, K.K. Bae, W.C. Cho, S.H. Kim, C.S. Park, Oxygen-carrier selection and thermal analysis of the chemical-looping process for hydrogen production, Int. J. Hydrog. Energy vol. 35 (22) (2010) 12246–12254, https://doi.org/10.1016/j.ijhydene.2010.08.043.
[29] Y. Ku, P.H. Lin, H.C. Wu, Y.C. Liu, Y.H. Tseng, H.Y. Lee, Preparation of Fe2O3/Al2O3 and Fe2O3/TiO2 pellets as oxygen carrier for chemical looping process, Aerosol Air Qual. Res vol. 17 (9) (2017) 2300–2309, https://doi.org/10.4209/aaqr.2017.03.0121.
[30] Y.C. Liu, Y. Ku, Y.H. Tseng, H.Y. Lee, Y.L. Kuo, Fabrication of Fe2O3/TiO2 oxygen carriers for chemical looping combustion and hydrogen generation, Aerosol Air Qual. Res vol. 16 (8) (2016) 2023–2032, https://doi.org/10.4209/aaqr.2015.10.0603.
[31] P.R. Kidambi, J.P.E. Cleeton, S.A. Scott, J.S. Dennis, C.D. Bohn, Interaction of iron oxide with alumina in a composite oxygen carrier during the production of hydrogen by chemical looping, Energy Fuels vol. 26 (1) (2012) 603–617, https://doi.org/10.1021/ef200859d.
[32] Y. Zhu, et al., La-hexaaluminate for synthesis gas generation by chemical looping partial oxidation of methane using CO_2 as sole oxidant, AIChE J. vol. 64 (2) (. 2018) 550–563, https://doi.org/10.1002/AIC.15942.
[33] L. Zhang, et al., Identifying the role of A-site cations in modulating oxygen capacity of iron-based perovskite for enhanced chemical looping methane-to-syngas conversion (Aug), ACS Catal. vol. 10 (16) (2020) 9420–9430, https://doi.org/10.1021/ACSCATAL.0C01811/ASSET/IMAGES/LARGE/CS0C01811_0010.JPEG.
[34] Z. Huang, et al., Exploration of reaction mechanisms on hydrogen production through chemical looping steam reforming using NiFe2O4 oxygen carrier, ACS Sustain. Chem. Eng. vol. 7 (13) (2019) 11621–11632, https://doi.org/10.1021/acssuschemeng.9b01557.
[35] G. Genchi, A. Carocci, G. Lauria, M.S. Sinicropi, Ijerph-17-00679-V3.Pdf, Int. J. Environ. Res. Public Health vol. 17 (3) (2020) 679–700.
[36] W. Liu, J.S. Dennis, S.A. Scott, The effect of addition of ZrO2 to Fe2O3 for hydrogen production by chemical looping, Ind. Eng. Chem. Res. vol. 51 (51) (2012) 16597–16609, https://doi.org/10.1021/ie302626x.
[37] N.S. Yüzbasi, et al., "ZrO2-Supported Fe2O3 for chemical-looping-based hydrogen production: effect of pH on its structure and performance as probed by X-ray absorption spectroscopy and electrical conductivity measurements, J. Phys. Chem. C. vol. 120 (34) (2016) 18977–18985, https://doi.org/10.1021/acs.jpcc.6b05276.
[38] L. Ma, et al., Efficient hydrogen production through the chemical looping redox cycle of YSZ supported iron oxides, Green. Energy Environ. vol. 6 (6) (2021) 875–883, https://doi.org/10.1016/j.gee.2020.06.023.
[39] R.H.J. Hannink, P.M. Kelly, B.C. Muddle, "Transformation Toughening in Zirconia-Containing Ceramics,", J. Am. Ceram. Soc. vol. 83 (3) (2004) 461–487, https://doi.org/10.1111/j.1151-2916.2000.tb01221.x.
[40] C.B. Abi, O.F. Emrullahoğlu, G. Said, "Microstructure and mechanical properties of MgO-stabilized ZrO2-Al2O3 dental composites,", J. Mech. Behav. Biomed. Mater. vol. 18 (2013) 123–131, https://doi.org/10.1016/j.jmbbm.2012.11.007.
[41] V.V. Galvita, H. Poelman, C. Detavernier, G.B. Marin, "Catalyst-assisted chemical looping for CO_2 conversion to CO,", Appl. Catal. B Environ. vol. 164 (2015) 184–191, https://doi.org/10.1016/j.apcatb.2014.09.007.
[42] S. Bock, R. Zacharias, V. Hacker, "High purity hydrogen production with a 10kWth RESC prototype system,", Energy Convers. Manag. vol. 172 (May) (2018) 418–427, https://doi.org/10.1016/j.enconman.2018.07.020.
[43] G. Witz, V. Shklover, W. Steurer, S. Bachegowda, H.P. Bossmann, Phase evolution in yttria-stabilized zirconia thermal barrier coatings studied by rietveld refinement of X-ray powder diffraction patterns, J. Am. Ceram. Soc. vol. 90 (9) (2007) 2935–2940, https://doi.org/10.1111/j.1551-2916.2007.01785.x.
[44] M.H. Bocanegra-Bernal, S.D. De La Torre, Phase transitions in zirconium dioxide and related materials for high performance engineering ceramics, J. Mater. Sci. vol. 37 (23) (2002) 4947–4971, https://doi.org/10.1023/A:1021099308957.
[45] J. Zhao, et al., Recoverable self-polarization in lead-free bismuth sodium titanate piezoelectric thin films, ACS Appl. Mater. Interfaces vol. 9 (34) (2017) 28716–28725, https://doi.org/10.1021/acsami.7b04033.
[46] J. Chevalier, S. Deville, E. Münch, R. Jullian, F. Lair, Critical effect of cubic phase on aging in 3 mol% yttria-stabilized zirconia ceramics for hip replacement prosthesis, Biomaterials vol. 25 (24) (2004) 5539–5545, https://doi.org/10.1016/J.BIOMATERIALS.2004.01.002.